Enhancement of Coherence Times in the Molecular Nanomagnet Cr_7Mn

Submitted to the
Department of Physics and Astronomy
in partial fulfillment of the
requirements for the degree of
Bachelors of Arts with honors.

By
Kai-Isaak Erich David Ellers

Advised by:
Professor Jonathan R. Friedman

May 7, 2019

Amherst College
Department of Physics and Astronomy

© 2019 Kai Ellers

Abstract

Over the last two decades, much effort has been invested in the development of quantum computing technologies, which are anticipated to be useful both in simulating complex quantum systems and in real-world applications such as cryptography. While some progress has been made in this area using physical systems such as trapped ions and superconducting devices, no system has yet been demonstrated that can be scaled up to a large enough number of qubits to be useful in most interesting applications. Molecular nanomagnets (MNMs) are promising systems for use as quantum bits (qubits) but are so far comparatively understudied in the context of such applications. Like any prospective qubits, MNM's must have a sufficiently long coherence time (T_2) to permit quantum logic operations. In this thesis we use spin-echo techniques to measure T_2 in the Cr_7Mn MNM and investigate several approaches to enhance T_2 in this system. Measurements are performed on Cr_7Mn samples diluted in toluene or benzene to concentrations between $10^{-6}\%$ and 1%, using a home-built electron-spin-resonance spectrometer at a range of temperatures and magnetic fields. We observe an enhancement of T_2 near zero magnetic field, providing strong evidence of an atomic-clock transition, where the dependence of the transition frequency on magnetic field vanishes to first order. We find that T_2 increases with decreasing concentration, at least at the clock transition. We also find that the rate of decoherence, $1/T_2$, increases linearly with temperature, with similar slopes but different vertical intercepts at and away from the clock transition. Finally, we find that T_2 can be enhanced by using Carr-Purcell-Meiboom-Gill pulse sequences to rephase the spins. These findings together suggest that both dipolar interactions and phonon mediated processes are factors limiting the coherence time in Cr_7Mn and demonstrate approaches to mitigate the effects of these sources of decoherence.

Acknowledgments

As in any scientific endeavor, there are so many people who have supported this project both directly and indirectly, and to whom I am deeply grateful. I would like to thank my mom, dad and sister for having gotten me this far; as a home-schooled student for most of my life it is especially true that so much of what I know is due directly to them and their continuous support and enthusiasm for my endeavors in physics and math have really kept me motivated. I am also deeply indebted to all my professors, both at Amherst and at Bowdoin College, who have taught me all I know about physics and whose enthusiasm has inspired me to pursue physics research. I would like to thank Brian Crepeau, Jim Kubasek and Misha Coggeshall-Burr, who have provided invaluable technical support at every stage of the project. And I would like to thank the group of Professor Richard Winpenny at University of Manchester for providing all the samples used in this project, and special thanks go to Grigore Timco for preparing the samples.

I would also like to thank my friends, fellow physics majors, and all those I have worked with in the lab over the years and especially Michael Cha, who falls into all three categories and has been fantastic company as we have pursued our theses together on the same equipment. In a similar vein, I am so grateful to Gajadhar Joshi and Professor Charles Collett, who have not only taught me so much about this project but have also contributed a tremendous amount themselves. Moreover, both have been wonderful to work with and have made my time on this project so fun and rewarding.

Finally I am extremely grateful to Professor Jonathan Friedman for taking me into his lab three years ago and supporting me all the way through my thesis. My first summer of research in Professor Friedman's lab was the perfect introduction to physics research and inspired me to keep going and pursue physics research as a career. He has taught me so much about my project and about physics in general over the years and I could not have asked for a better

mentor and adviser.

I acknowledge and thank Amherst College for being a wonderful home for the last four years and for providing funding for me to work on my thesis during the summer through the Gregory S. Call fellowship. Thank you also to the U.S. National Science Foundation for supporting this research through Grant No. DMR-1708692.

Contents

List of Figures

Chapter 1

Introduction

1.1 Motivation: Quantum Computation

The emerging field of quantum information has received much attention recently for its potential applications both in physics research and in numerous other fields with immediate real-world applications. In physics, quantum simulation would enable the theoretical study of interesting physical systems too complex for current classical computers to solve. Meanwhile, much theoretical progress has been made in developing quantum computing algorithms that would allow exponential speed-ups in classically hard problems, with the most famous example being Shor's algorithm for factorization of large numbers. This latter development would have important applications not only to theoretical problems in number theory but also in cryptography, where most modern encryption algorithms rely on knowing the prime factors of numbers too large to factor with current computing technology.

To understand the advantages bestowed by a quantum computer, and to get some idea of what might go into realizing such a device, it is helpful to understand what distinguishes a quantum computer from its classical analogue. The fundamental unit of information storage in a classical computer is the bit, which is simply a classical two-state system whose states, denoted 0 and 1, can be controlled and measured at will. The quantum analogue of a bit is called a quantum bit or qubit, and is a two-state quantum system, with states denoted by $|0\rangle$ and $|1\rangle$. But as a quantum system, a qubit can also be in any arbitrary quantum superposition of the states $|0\rangle$ and $|1\rangle$ and we can denote such a state by $\alpha|0\rangle + \beta|1\rangle$, where α, β are any complex numbers satisfying $|\alpha|^2 + |\beta|^2 = 1$. The advantage of using qubits becomes apparent when we consider a system with two or more bits: A system of two classical bits can be in any of the four states 00, 01, 10 or 11, and in an arbitrary state of a system with N classical bits, the state of each bit can encode exactly one piece of information so that the system as a whole can store N pieces of information in a given state. A system of two qubits, on the other hand, can be in any arbitrary state $\alpha|00\rangle + \beta|01\rangle + \gamma|10\rangle + \delta|11\rangle$. In a general system of N qubits, then, one can store 2^{N-1} pieces of information, giving an exponential improvement in information storage capacity over a classical computer.

Before one can reap the benefits of quantum computation, however, one must identify an actual physical system that can be used as a qubit and demonstrate that such qubits can be combined to make multi-qubit quantum logic gates and ultimately a functional quantum computer. In the last three decades, much effort has been invested in this area, both by experimentalists identify-

ing and developing physical systems to be used as qubits [4] and by theorists developing quantum error correcting codes [5] to correct for errors in realistic operations. In the former pursuit, many groups have already built small ($\sim$10 qubit) quantum computers using trapped ions, quantum dots or superconductors as qubits [6–8] and successfully demonstrated simple quantum algorithms, including simulations of simple molecules like H_2 [9]. In this thesis, I investigate the viability of a relatively understudied potential qubit system, namely molecular nanomagnets (MNMs).

Any quantum logic gate must necessarily operate over a finite amount of time, so in order to perform multiple gates in succession, as is required in a functional quantum computer, one's qubit systems must remain coherent long enough to allow the gate operations to be completed without losing information. The time scale over which a system remains coherent is referred to as its coherence time and denoted by T_2 (see section 3.4). Coherence times have been investigated in many prospective qubit systems [4], and in this thesis I perform measurements of T_2 in the MNM Cr_7Mn and explore several methods to enhance T_2 in this system. Previous work, which will be described in more detail in the next section, has already examined coherence times in some other MNMs and Single Molecule Magnets (SMMs) and demonstrated that T_2 can be enhanced in these systems by sample dilution and deuteration [10] and by working at an atomic-clock transition [11]. I explore some of these approaches in Cr_7Mn as well as dynamical decoupling techniques that have been extensively employed in nuclear magnetic resonance (NMR), and electron spin resonance (ESR) experiments.

1.2 Overview of Approaches to Enhancing Coherence Time

While an isolated two-state quantum system will evolve with time in a very predictable way according to the rules of quantum mechanics, any interaction between the system and its environment will result in the system's time-evolution becoming unpredictable. Put another way, unless we can fully characterize a quantum system's environment, we cannot exactly predict how the system's state will evolve in time and therefore we will gradually lose information about the system's state as time passes. This process is referred to as decoherence and for many applications, including quantum computing, it is imperative to reduce the rate of decoherence in constituent systems as much as possible so as to make their evolution as coherent as possible. In designing a quantum computer then, it is desirable to reduce interactions between our individual qubits and their environment, while some specific, well-controlled interactions with other qubits will be required if we are to construct multi-qubit logic gates. The coherence time, T_2, introduced in the previous section provides a quantitative measure of the decoherence rate as demonstrated in chapter 3.

There are many ways in which a quantum system can interact with its environment and the first step in enhancing coherence time in qubits is to lower the qubits' temperature so as to reduce thermal fluctuations. In order to reduce thermal effects sufficiently to make T_2 measurable with our and similar apparatus, MNM samples must be cooled to temperatures on the order of a few Kelvin.

One major source of decoherence comes from dipolar interactions between electron spins and nearby magnetic moments [10] and there are several possible avenues available for reducing the deleterious effects of these interactions on T_2. The strength of these dipolar interactions in a sample will generally decrease with the distance between molecules, so one way to decrease the effect of interactions is to dilute the MNM sample in some non-magnetic matrix. Ardavan *et al.* [10] studied T_2 in a sample of the MNM Cr_7Ni and found that by diluting samples in toluene they were able to achieve T_2 times up to 0.55 μs at 1.8 K.

A second approach used by Ardavan *et al.* in Cr_7Ni is to use deuterated MNM samples, in which ^{1}H nuclei in the sample are replaced with ^{2}D nuclei, which have a magnetic moment approximately six times smaller than ^{1}H [10]. Because of this smaller magnetic moment, the use of deuterated samples would be expected to increase coherence time if T_2 is limited by interactions between the MNM spins and protons in the ^{1}H nucleus. Indeed, Ardavan *et al.* found an increase in T_2 by a factor of 6-7 in deuterated samples as compared with hydrogenated samples, reaching a maximum value of 1.38 μs at 1.8 K.

Another possible approach to increase coherence time in MNMs is to work at an atomic-clock transition (see section 1.4), as demonstrated by Shiddiq *et al.* in the MNM HoW_{10} [11]. Atomic-clock transitions get their name from their application in atomic clocks, in which they are used to obtain a steady clock frequency, but the principle (explained in section 1.4) can be used more generally to reduce the sensitivity of physical systems to fluctuations in their environment. HoW_{10} and some other MNMs exhibit atomic-clock transitions

when an external magnetic field of some particular (predictable) strength is applied to the sample and Shiddiq *et al.* used this method to measure T_2 in HoW_{10} both at and away from a clock transition. Working at 5.0 K, Shiddiq *et al.* found T_2 values of approximately 1.5 μs away from the clock transition and 8.4 μs at the clock transition, giving an increase in T_2 by a factor of 5-6 times. Notably, Shiddiq *et al.* achieved this result without working in the dilute limit in which T_2 is expected to be optimized.

Finally, there are a number of techniques such as Carr-Purcell-Meiboom-Gill (CPMG) and Dynamical Decoupling (DD) that have been developed extensively in Nuclear Magnetic Resonance (NMR) experiments and can be easily adapted into our ESR experiments. In the most basic spin-echo experiment, a sequence of just two EM radiation pulses is applied and the time between pulses is varied to measure T_2. In a CPMG experiment, on the other hand, a much longer sequence of tens of pulses is applied and signal from the sample is measured after each additional pulse, as described in detail in section 3.5. CPMG and DD techniques have in fact already been demonstrated to be effective in increasing T_2 in spin-based qubits, for example by Medford *et al.*, who found T_2 to increase with the number of pulses according to a power law [12].

All of the techniques mentioned in this section can be applied to our Cr_7Mn system and much of the remainder of this thesis will be devoted to documenting their implementation and efficacy in increasing coherence time.

1.3 Molecular Nanomagnets

Molecular nanomagnets are a class of molecules characterized by the fact that each molecule possesses a magnetic moment, and these systems exhibit a number of properties that make them both potentially useful in quantum computing applications and inherently interesting physical systems to study. Firstly, MNM's are highly chemically engineerable, allowing their properties to be tailored to specific applications of interest [13]. Secondly, individual MNM molecules are decidedly microscopic systems and thus exhibit quantum mechanical behavior that cannot be seen in classical systems. Yet we can prepare samples of large numbers ($\sim 10^{15}$) of MNM's and study the behavior of individual molecules by interacting with the sample as a whole. This latter property has already been demonstrated to be useful in designing a quantum computer by the successful implementation of small NMR-based quantum computers working under the same principal [14].

MNM's have been studied extensively since the 1990's, motivated both by their potential applications in quantum information processing and magnetic memory [15–18] and by their inherent interest as systems that span the realms of quantum mechanics and classical (macroscopic) physics [15, 19]. Such studies have made use of a diverse range of experimental techniques [20] such as Electron Paramagnetic Resonance (EPR) spectroscopy [1, 10, 11, 19, 21] and Inelastic Neutron Scattering (INS) [22]. Such studies on MNM's have ranged from measurements of coherence times [1, 10, 11] and other characterization [19] to demonstrations of interesting physical phenomena such as quantum tunneling of magnetization [23] and quantum phase interference [24], among

many other areas of research.

I have worked with the MNM Cr_7Mn (Figure 1.1), which is obtained from the diamagnetic ring Cr_8 by replacing one Cr^{3+} ion with a Mn^{2+} ion, giving a total spin $s = 1$ [10]. The system can be described by the Hamiltonian

$$\hat{H} = -DS_z^2 + E(S_x^2 - S_y^2) + g\mu_B \vec{B} \cdot \vec{S}, \tag{1.1}$$

where D = 21 GHz, E = 1.9 GHz and g = 1.96 is the Landé g-factor and μ_B is the Bohr magneton [1]. The third term in this Hamiltonian is the Zeeman term, which gives the magnetic-field dependence of all the states, while the first two terms describe the molecule's longitudinal and transverse anisotropies, respectively. This Hamiltonian gives rise to the three energy eigenstates shown in Figure 1.2, which are well-described by spin quantum numbers $m = 0$ and $m = \pm 1$ away from zero magnetic field. Near zero field, the transverse anisotropy term results in a zero-field splitting between the two lowest-energy states, giving superposition states $|\pm\rangle = \frac{1}{\sqrt{2}}(|+1\rangle \pm |-1\rangle)$. In addition, Figure 1.2 shows that the three states have different dependence on magnetic field due to the Zeeman term and that the two lowest-energy states are shifted down by the longitudinal anisotropy term. In chapter 2 we will show how the Hamiltonian (Eq. 1.1) can give us an effective two-state system near zero-field, consisting of just the $|\pm\rangle$ states. This enables us to use Cr_7Mn as a qubit, provided it has a sufficiently long coherence time to allow gate operations to be performed.

In addition to engineering parameters of individual molecules, techniques

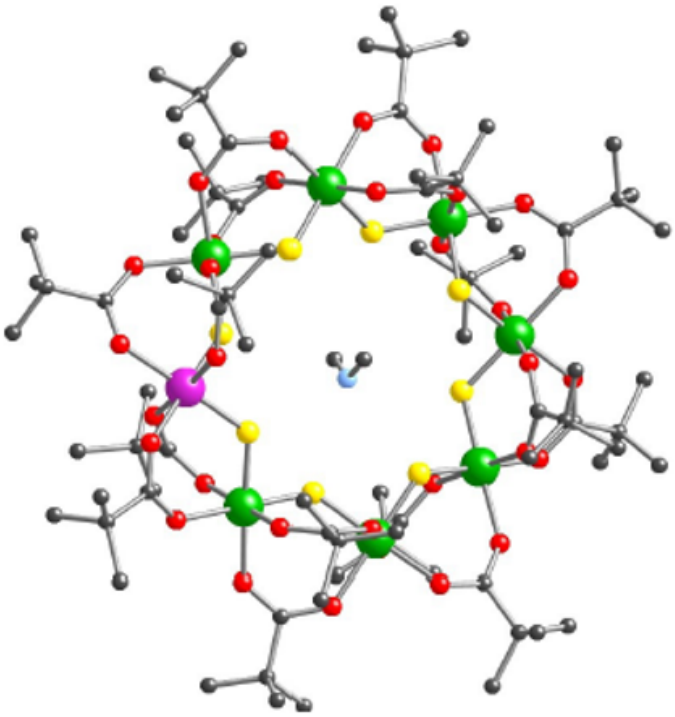

Figure 1.1: Cr_7Mn molecular structure, showing seven Cr^{3+} ions (green) and one Mn^{2+} ion (purple). Taken from [1] with permission.

have also been developed to create dimers of two MNM molecules (Figure 1.3), so that the Hamiltonian for the system as a whole includes a coupling term J_{12} linking the two molecules in the dimer. Thus if we define

$$\hat{H}_i = -DS_{z,i}^2 + E(S_{x,i}^2 - S_{y,i}^2) + g\mu_B \overrightarrow{B} \cdot \overrightarrow{S_i}, \tag{1.2}$$

for $i = 1, 2$, then the total Hamiltonian for the dimer is:

$$\hat{H}_{dimer} = \hat{H}_1 + \hat{H}_2 + J_{12} \overrightarrow{S}_1 \cdot \overrightarrow{S}_1. \tag{1.3}$$

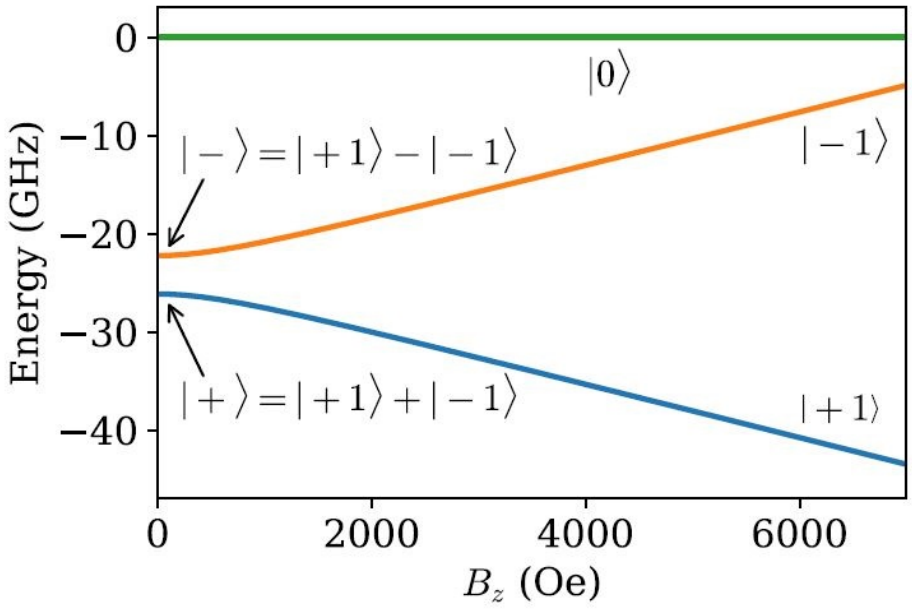

Figure 1.2: Energy-level diagram for Cr_7Mn showing the $|0\rangle$ and $|\pm 1\rangle$ states, as well as mixed states $|\pm\rangle$ near an avoided crossing at zero external magnetic field. Taken from [1] with permission.

Such dimers have already been studied for their potential applications in quantum information processing [25, 26]. The coupling term between molecules in a dimer provides a means by which the evolution of the state of one molecule can be affected by the state of the other molecule allowing for execution of two-qubit gates such as a CNOT gate. More precisely, the coupling between molecules will slightly shift the energy levels, and hence transition frequency, of one molecule and the sign of this shift will depend on the second molecule's state. Thus the state of molecule 1 in the dimer will evolve differently depending on the state of molecule 2 in the presence of a coupling term J_{12}. Additionally, we can still address each molecule individually (i.e. execute single-qubit gates) as long as the two molecules have different transition frequencies to

start with. This is made possible by the use of heterodimers, where the two coupled molecules are slightly different variants of the Cr_7Mn molecule with different resonant frequencies. The techniques used to implement two-qubit gates with such a heterodimer are similar to well-established techniques for NMR quantum computers as described in [14].

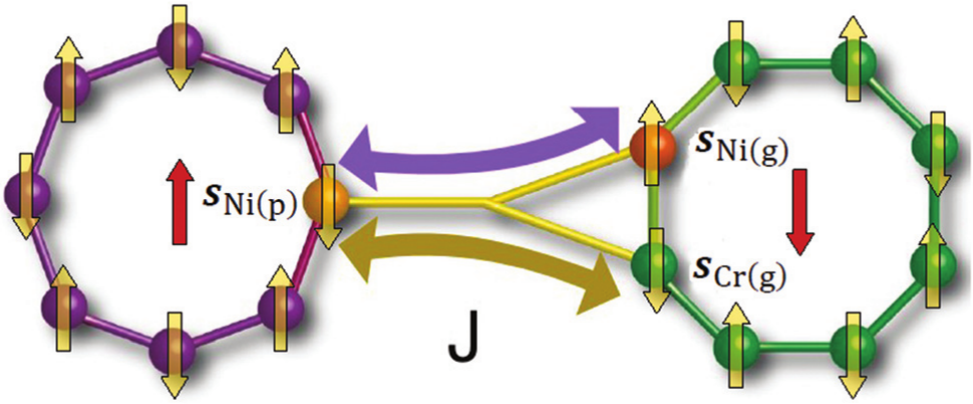

Figure 1.3: Two slightly different variants of our Cr_7Mn molecule, linked by chemical bonds that give rise to a coupling term in the system Hamiltonian. Taken from [2] with permission.

1.4 Introduction to Atomic-clock Transitions

In designing a clock, we must identify a system that can provide a reliable frequency to be used as the clock frequency and one common method is to make use of some two-level system, in which the energy difference between the two states determines the clock frequency. In order to make such a clock very precise, it is imperative to reduce the sensitivity of the transition frequency to environmental fluctuations; one way to do this is to work at an atomic-clock transition, so named for its use in precisely this application.

In general, the energy of both states under consideration will depend on environmental parameters, so that any change in one of these parameters will slightly alter the transition frequency and render the clock correspondingly less reliable. However, it may be the case that the energy difference between the states passes through a local extremum at some parameter value. When this happens, the energy difference between the states, and hence the transition frequency, becomes independent of that parameter to first order, resulting in a much more stable clock frequency and hence a more reliable clock. Any transition with the property that the transition frequency is to first order independent of some external parameter is referred to as an atomic-clock transition, and this concept is of great utility in atomic clocks and other applications where a stable frequency is required.

As discussed in section 1.2, we would like to identify physical systems to be used as qubits that are relatively insensitive to fluctuations in their environment so as to maximize the coherence time, T_2, of the system. Atomic-clock transitions can be used to achieve this goal. Figure 1.2 shows the energy-level diagram for Cr_7Mn; as discussed already, we can work with an effective spin-1/2 system of the two lowest-energy states. As Figure 1.2 shows, there is an avoided crossing of these states near zero-magnetic field resulting in superposition states $|\pm\rangle = \frac{1}{\sqrt{2}}(|+1\rangle \pm |-1\rangle)$, and the energy of both states becomes flat around zero field. Thus the first derivative of the energy difference between these states will go to zero at zero field, and hence the transition frequency between the two states will be independent of magnetic field to first order.

As mentioned in section 1.2, dipole interactions with nearby nuclear spins are likely to be a significant source of decoherence in our system as they will change the local magnetic field seen by individual spins. However, since the frequency of each spin is to first order independent of magnetic field at the clock transition, any small fluctuations in magnetic field due to nearby spins will not substantially affect each spin's frequency when we are working at the clock transition. In this way we can make our ensemble of spins relatively immune to decoherence caused by other spins, thus reducing a potentially significant source of decoherence. This approach was employed by Shiddiq *et al.* [11] in the HoW_{10} MNM and one of the major goals of this project was to apply the same strategy in Cr_7Mn.

Chapter 2

Theory

Before describing the experiments we conducted, it is important to give a theoretical foundation for our work by describing the basic quantum mechanics underlying our experiments. As described in section 1.3, our Cr_7Mn molecule can be treated as a spin-1 system at sufficiently low temperatures. Near zero magnetic field, the two lowest eigenstates have an avoided crossing, resulting in energy eigenstates $|\pm\rangle = \frac{1}{\sqrt{2}}(|+1\rangle \pm |-1\rangle)$. We begin by describing the dynamics of a generalized two-state system in an applied magnetic field and we then show how our states result in an effective two-state system.

2.1 Magnetic Resonance

We will start by considering the phenomenon of magnetic resonance in a spin-1/2 system. We can write the spin state of a spin-1/2 system in the $\hat{S}_z$ basis as $|\psi\rangle = a\,|+z\rangle + b\,|-z\rangle$, where $a, b \in \mathbb{C}$ and we can therefore represent its spin state as a unit vector in $\mathbb{R}^3$. The collection of possible endpoints of these

vectors form a unit sphere, which we refer to as the Bloch sphere. One can show[1] that in the presence of a constant longitudinal magnetic field $\mathbf{B} = B_0\hat{z}$, the spin will precess about the z axis with frequency $\omega_0 = \gamma B_0 = g\mu_B B_0$, where $\gamma = g\mu_B$ is the gyromagnetic ratio of the system, g is the Landé g-factor and μ_B is the Bohr magneton.

Now suppose we additionally apply an oscillating transverse field to our sample, so that the full external magnetic field is $\mathbf{B} = B_1\cos(\omega t)\hat{x} + B_0\hat{z}$. Then the Hamiltonian for our system is

$$\hat{H} = -\vec{\mu}\cdot\vec{B} = \gamma\hat{\mathbf{S}}\cdot(B_1\cos(\omega t)\hat{x} + B_0\hat{z}) = \omega_0\hat{S}_z + \omega_1\cos(\omega t)\hat{S}_x, \tag{2.1}$$

where μ is the system's magnetic moment and we have defined $\omega_1 = \gamma B_1$, which has units of frequency. Note that the $\hat{S}_x$ term in (2.1) couples the $|+z\rangle$ and $|-z\rangle$ states as we can easily calculate:

$$\langle +z|\hat{S}_x|-z\rangle = \frac{1}{2}. \tag{2.2}$$

Since the Hamiltonian 2.1 is time dependent, we must resort directly to Schrödinger's equation to solve for the system's dynamics:

$$\hat{H}\,|\psi(t)\rangle = i\frac{d\,|\psi(t)\rangle}{dt}. \tag{2.3}$$

Let us suppose the particle is prepared to be initially spin up along the z

[1] See, for example, section 4.3 of [27].

axis. Then in the $\hat{S}_z$ basis we can write

$$|\psi(0)\rangle = \begin{pmatrix} 1 \\ 0 \end{pmatrix} \tag{2.4}$$

for the initial state of the system and

$$|\psi(t)\rangle = \begin{pmatrix} a(t) \\ b(t) \end{pmatrix} \tag{2.5}$$

for its state at any later time t. Substituting 2.5 into the Schrödinger equation 2.3, we get the system of differential equations

$$\frac{1}{2}\begin{pmatrix} \omega_0 & \omega_1\cos(\omega t) \\ \omega_1\cos(\omega t) & -\omega_0 \end{pmatrix}\begin{pmatrix} a(t) \\ b(t) \end{pmatrix} = i\begin{pmatrix} \dot{a}(t) \\ \dot{b}(t) \end{pmatrix}, \tag{2.6}$$

and from this and initial condition 2.4 it can be shown[2] that the probability of measuring the particle spin down along the z axis subsequently oscillates with time, and that in the case $\omega = \omega_0$, we get

$$|\langle -z|\psi(t)\rangle|^2 = \sin^2(\frac{\omega_1 t}{4}). \tag{2.7}$$

If the frequencies ω and ω_0 are not exactly matched, it can be shown that the probability will still oscillate with time, as given by Rabi's formula:

$$|\langle -z|\psi(t)\rangle|^2 = \frac{\omega_1^2/4}{(\omega_0-\omega)^2+\omega_1^2/4}\sin^2(\frac{\sqrt{(\omega_0-\omega)^2+\omega_1^2/4}}{2}t). \tag{2.8}$$

[2]See section 4.4 of [27].

2.2 Cr_7Mn as an Effective Two-State System

At the temperatures we work at ($\sim 2K$), Cr_7Mn can be considered as an $S = 1$ system. Recall from section 1.3 that the Hamiltonian for our system is

$$\hat{H} = -DS_z^2 + E(S_x^2 - S_y^2) + g\mu_B \vec{B} \cdot \vec{S}, \tag{2.9}$$

where $D = 21$ GHz, $E = 1.9$ GHz, $g = 1.96$ is the Landé g-factor and μ_B is the Bohr magneton [1]. We will show when the external magnetic field is zero, the states $|0\rangle$ and $|\pm\rangle = \frac{1}{\sqrt{2}}(|+1\rangle \pm |-1\rangle)$ are eigenstates of this Hamiltonian and that the spin operators $\hat{S}_x, \hat{S}_y$ and $\hat{S}_z$ each couples one pair of the states $|+\rangle, |-\rangle$ and $|0\rangle$ while annihilating the third state.

To show this, we start by expressing $\hat{S}_x, \hat{S}_y, \hat{S}_z$ in the basis $\{|+1\rangle, |0\rangle, |-1\rangle\}$, the eigenstates of $\hat{S}_z$,

$$\hat{S}_x = \frac{1}{\sqrt{2}} \begin{pmatrix} 0 & 1 & 0 \\ 1 & 0 & 1 \\ 0 & 1 & 0 \end{pmatrix} ; \; \hat{S}_y = \frac{1}{\sqrt{2}} \begin{pmatrix} 0 & -i & 0 \\ i & 0 & -i \\ 0 & i & 0 \end{pmatrix} ; \; \hat{S}_z = \begin{pmatrix} 1 & 0 & 0 \\ 0 & 0 & 0 \\ 0 & 0 & -1 \end{pmatrix}. \tag{2.10}$$

Now expressing $|+\rangle, |-\rangle$, and $|0\rangle$ in the same basis, we get

$$|+\rangle = \frac{1}{\sqrt{2}} \begin{pmatrix} 1 \\ 0 \\ 1 \end{pmatrix} ; \; |0\rangle = \begin{pmatrix} 0 \\ 1 \\ 0 \end{pmatrix} ; \; |-\rangle = \frac{1}{\sqrt{2}} \begin{pmatrix} 1 \\ 0 \\ -1 \end{pmatrix}. \tag{2.11}$$

From 2.10 and 2.11 we see that

$$\hat{S}_z \left|+\right\rangle = \begin{pmatrix} 1 & 0 & 0 \\ 0 & 0 & 0 \\ 0 & 0 & -1 \end{pmatrix} \frac{1}{\sqrt{2}} \begin{pmatrix} 1 \\ 0 \\ 1 \end{pmatrix} = \frac{1}{\sqrt{2}} \begin{pmatrix} 1 \\ 0 \\ -1 \end{pmatrix} = \left|-\right\rangle, \tag{2.12}$$

and similarly we can work out that

$$\hat{S}_z \left|-\right\rangle = \left|+\right\rangle ; \hat{S}_z \left|0\right\rangle = 0, \tag{2.13}$$

$$\hat{S}_x \left|+\right\rangle = \left|0\right\rangle ; \ \hat{S}_x \left|-\right\rangle = 0; \ \hat{S}_x \left|0\right\rangle = \left|+\right\rangle, \tag{2.14}$$

$$\hat{S}_y \left|+\right\rangle = 0; \ \hat{S}_y \left|-\right\rangle = i \left|0\right\rangle ; \ \hat{S}_y \left|0\right\rangle = -i \left|-\right\rangle. \tag{2.15}$$

Equations 2.12 through 2.15 tell us that the operators $\hat{S}_x, \hat{S}_y, \hat{S}_z$ each exchanges two of the states $\left|+\right\rangle, \left|-\right\rangle, \left|0\right\rangle$ while annihilating the third state, as promised. Applying each of these operators a second time gives us

$$\hat{S}_z^2 \left|+\right\rangle = \left|+\right\rangle ; \hat{S}_z^2 \left|-\right\rangle = \left|-\right\rangle ; \hat{S}_z^2 \left|0\right\rangle = 0, \tag{2.16}$$

$$\hat{S}_x^2 \left|+\right\rangle = \left|+\right\rangle ; \ \hat{S}_x^2 \left|-\right\rangle = 0; \ \hat{S}_x^2 \left|0\right\rangle = \left|0\right\rangle, \tag{2.17}$$

$$\hat{S}_y^2 \left|+\right\rangle = 0; \ \hat{S}_y^2 \left|-\right\rangle = \left|-\right\rangle ; \ \hat{S}_y^2 \left|0\right\rangle = \left|0\right\rangle. \tag{2.18}$$

From equations 2.16 through 2.18, we can see that the states $\left|+\right\rangle, \left|-\right\rangle, \left|0\right\rangle$ are eigenstates of 2.9 with $\mathbf{B} = 0$, since in that case we have

$$\hat{H} \left|+\right\rangle = (-D + E) \left|+\right\rangle ; \tag{2.19}$$

$$\hat{H}\,|-\rangle = (-D - E)\,|-\rangle\,; \tag{2.20}$$

$$\hat{H}\,|0\rangle = 0. \tag{2.21}$$

Now suppose we apply an external radiation field $\mathbf{B} = B_1 \cos(\omega t)\hat{z}$. Then the Hamiltonian 2.9 becomes

$$\hat{H} = -DS_z^2 + E(S_x^2 - S_y^2) + g\mu_B B_1 \cos(\omega t)\hat{S}_z, \tag{2.22}$$

Then, similarly to equation 2.2, we can calculate from 2.13 that

$$\langle +|\hat{S}_z|-\rangle = 1, \tag{2.23}$$

which shows that $\hat{S}_z$ couples only these two states, and that the coupling strength is twice that in 2.2. So since $|+\rangle$ and $|-\rangle$ are eigenstates of the zero-field Hamiltonian, we see that if our initial state is any linear combination of $|+\rangle$ or $|-\rangle$, then the state at any future time t must also be a linear combination of these two. In particular, suppose our initial state is $\psi(0) = |+\rangle$. Then we can work in the subspace spanned by $|+\rangle$ and $|-\rangle$ and express the initial and subsequent states of the system as

$$|\psi(0)\rangle = \begin{pmatrix} 1 \\ 0 \end{pmatrix}\,;\ |\psi(t)\rangle = \begin{pmatrix} a(t) \\ b(t) \end{pmatrix}. \tag{2.24}$$

In this basis, we can use equations 2.12, 2.13, 2.19 and 2.20 to write the

Hamiltonian 2.22 as

$$\hat{H} = \begin{pmatrix} -D+E & 0 \\ 0 & -D-E \end{pmatrix} + \begin{pmatrix} 0 & g\mu_B B_1 \cos(\omega t) \\ g\mu_B B_1 \cos(\omega t) & 0 \end{pmatrix} \tag{2.25}$$

Now recall that the gyromagnetic ratio is $\gamma = g\mu_B$, and let us define the following two quantities with units of frequency:

$$\omega_1 = 2\gamma B_1, \tag{2.26}$$

$$\omega_0 = 2E. \tag{2.27}$$

With these substitutions, plugging 2.25 into the Schrödinger equation gives

$$\frac{1}{2} \begin{pmatrix} -2D+\omega_0 & \omega_1 \cos(\omega t) \\ \omega_1 \cos(\omega t) & -2D-\omega_0 \end{pmatrix} \begin{pmatrix} a(t) \\ b(t) \end{pmatrix} = i \begin{pmatrix} \dot{a}(t) \\ \dot{b}(t) \end{pmatrix} \tag{2.28}$$

This is identical to 2.6 except for the terms involving D, which will not change the solutions since they simply amount to adding $-2D$ times the identity matrix to the equation. Then equation 2.28 and 2.6 are identical, leading us to conclude that our Cr_7Mn molecule will behave as a two-state system provided the initial state is a linear combination of the $|+\rangle$ and $|-\rangle$ states. Thus, in analogy with 2.7 we must have

$$|\langle -|\psi(t)\rangle|^2 = \sin^2(\frac{\omega_1 t}{4}). \tag{2.29}$$

This also implies that

$$|\langle +|\psi(t)\rangle|^2 = \cos^2(\frac{\omega_1 t}{4}), \tag{2.30}$$

and of course the analogue of Rabi's formula (2.8) also holds for this system as well. These results show that in the presence of an external oscillating magnetic field the probabilities of measuring the system in the $|+\rangle$ and $|-\rangle$ states oscillate sinusoidally with time, a phenomenon which we refer to as Rabi oscillation. They also show that if we want to drive Rabi oscillations between the states $|+\rangle$ and $|-\rangle$, then we should apply a longitudinal RF magnetic field oscillating with frequency $\omega = \omega_0 = 2E$. Using a double angle formula, we can also write 2.30 as

$$|\langle +|\psi(t)\rangle|^2 = \frac{1}{2}(1 + \cos\left(\frac{\omega_1 t}{2}\right)). \tag{2.31}$$

Thus if we can measure the frequency $\omega_R = \omega_1/2$ of Rabi oscillations in our system, then equation 2.26 gives the amplitude of the oscillating magnetic field:

$$B_1 = \frac{\omega_1}{2\gamma} = \frac{\omega_R}{\gamma}. \tag{2.32}$$

There is one more observation we should make about the behavior of our system as an effective two-state system. We remarked in section 2.1 that in addition to oscillating between the $|+z\rangle$ and $|-z\rangle$ basis states in the presence of a transverse oscillating magnetic field, a two-state system will also precess about the z axis with frequency $\omega_0 = \gamma B_0$ in the presence of a constant longitudinal magnetic field $\mathbf{B} = B_0\hat{z}$. We see from equation 2.28 that the zero-field Hamiltonian acts on the basis states $|\pm\rangle$ in exactly the same way

that a longitudinal magnetic field acts on the basis states $|\pm z\rangle$ for the spin-1/2 system. This shows that under the full Hamiltonian 2.22, our system should undergo some kind of analogous precession. We can show, however, that each of the eigenstates of the Cr_7Mn Hamiltonian has no magnetic moment, that is $\langle S_\alpha \rangle = 0$ for $\alpha = x, y, z$. Hence it cannot be an actual magnetic moment that precesses about the axis aligned with $|+\rangle$. For an actual two state system, the precession will also correspond to an oscillating probability of measuring the system in the states $\frac{1}{\sqrt{2}}(|+z\rangle \pm |-z\rangle) = |\pm x\rangle$. The analogous result in our effective two-state system is that the probability of measuring the system in the states $\frac{1}{\sqrt{2}}(|+\rangle \pm |-\rangle) = |\pm 1\rangle$ will oscillate with frequency $\omega_0 = 2E$. Thus if we picture the $|\pm\rangle$ states as defining the vertical axis of the Bloch sphere, the spin state of the effective two-state system will still precess about the $|+\rangle$ axis. Since the $|\pm 1\rangle$ have a nonzero magnetic moment, this precession will induce an EMF in a nearby antenna, allowing us to make measurements of the system's state.

Chapter 3

Experimental Apparatus and Techniques

As described in chapter 1, we want to make measurements on our MNM samples by driving transitions between two energy eigenstates. The properties we are trying to measure are expected to depend on temperature and magnetic field, among other factors. Therefore, we need an experimental apparatus that will allow us to interact with our sample and control these external parameters reliably. To make our measurements we have used a home-built ESR spectrometer, including a commercial Arbitrary Waveform Generator (AWG) as a signal source, to generate radio frequency electromagnetic pulses to probe our sample, and we have used loop-gap resonators (LGR's) to concentrate these pulses at the location of our sample. We have used a Physical Property Measurement System (PPMS) to control the external parameters, namely temperature and magnetic field. This chapter describes these systems in detail,

as well as describing the phenomenon of spin echo, which is central to all experiments described in this thesis.

3.1 Physical Property Measurement System

We have used an apparatus manufactured by Quantum Design, called the Physical Property Measurement System, to control temperature and magnetic field in our experiments. It consists of a probe suspended in a liquid helium bath inside a thermally insulating dewar, as shown in Figures 3.1 and 3.2. The dewar insulation consists of a reflective super-insulating layer and a liquid nitrogen jacket to reduce the boil-off rate of heilum. The sample chamber can be set to any temperature between 1.7 K and 400 K and the temperature is generally stable as long as it is not set below 1.8 K.

Magnetic-field control in the PPMS is achieved using a superconducting magnet, which can produce a constant field up to 9 T and can also be ramped continuously at any rate between 10.8 Oe/s and 199.9 Oe/s. However, we found that the field control provided by the PPMS current source was not sufficiently fine for our measurements, and consequently we have been using an Agilent DC power supply to "charge" the superconducting magnet, while still using the PPMS to control temperature. To make measurements, we position our samples inside a copper shield at the end of the probe, which is then suspended inside the PPMS sample chamber.

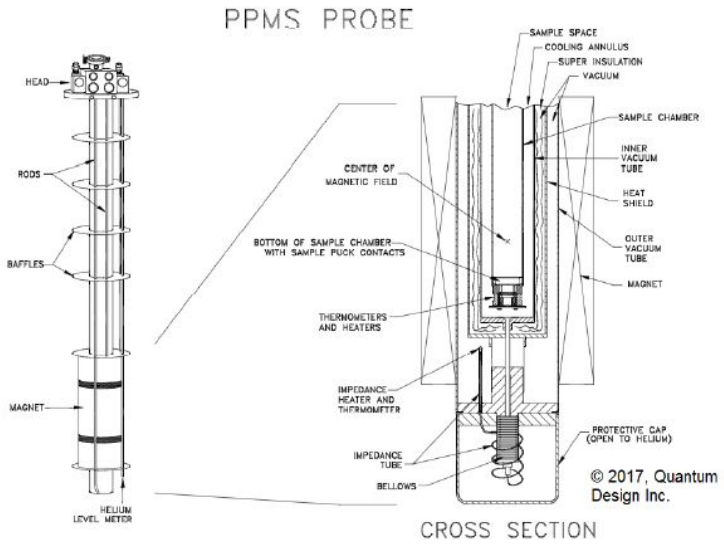

Figure 3.1: Diagram of the PPMS probe design. Taken from PPMS Hardware Manual with permission [3].

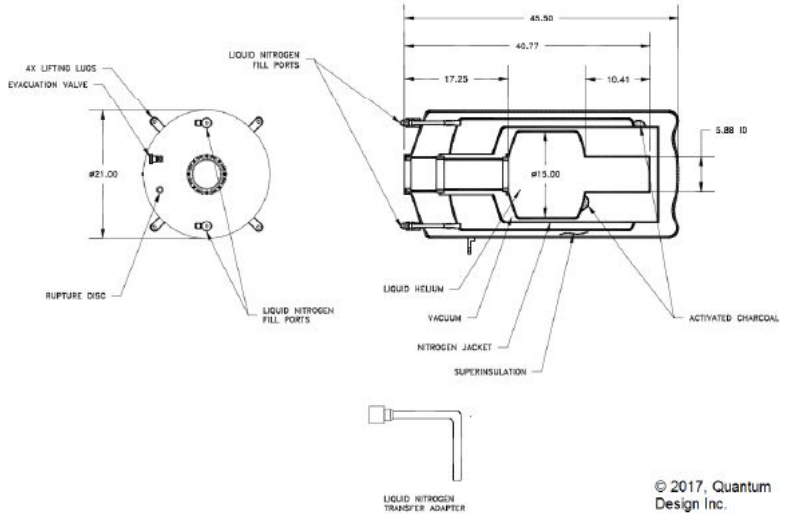

Figure 3.2: Diagram of the PPMS dewar. Taken from PPMS Hardware Manual with permission [3].

3.2 Electron Spin Resonance Spectrometer and Sampling Theory

The spectrometer used in our measurements is home built and has been continuously evolving over the course of this project, but the essential hardware, shown in Figure 3.3, has been nearly constant throughout. A block diagram of the essential components of our circuit is shown in Figure 3.4. However, before acquiring the Arbitrary Waveform Generator (AWG) we instead used a CW signal source to produce an RF signal and created pulses by putting the output through hardware switches. In order to drive the transition between energy eigenstates of our samples, we need to produce short ($\sim$100 ns) pulses at a frequency approximately matched to the energy-level splitting, which is around 4 GHz.

Our initial setup used an Agilent signal source to produce a continuous-wave (CW) radio-frequency (RF) signal, which was then split to produce two outputs, each with an identical frequency to the original. One of these was used as the reference for an IQ mixer, while the other was fed into a hardware switch, controlled by a Field Programmable Gate Array (FPGA), to produce RF pulses. The pulse amplitude was controlled by a large ($\sim$20 dBm) amplifier and variable attenuator (also controlled by the FPGA) and passed through 1 GHz-bandwidth bandpass filters, primarily to remove noise injected by the switch. The pulses were then fed to the sample by means of a circulator, which passes the input to the sample chamber (via cables attached at the probe head). The returning signal was amplified and fed into the second input

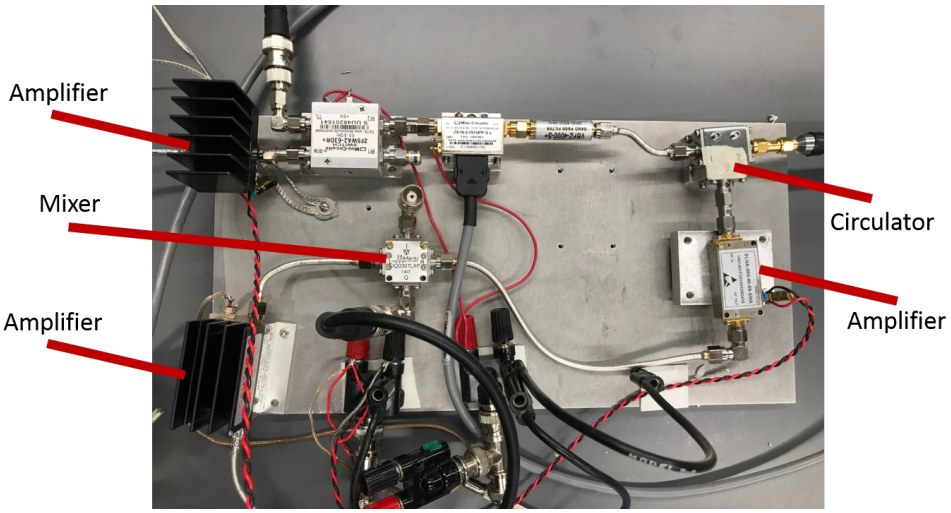

Figure 3.3: The essential hardware components used in our spectrometer.

of the mixer, with the possibility of tuning the relative phase of the two inputs by hand using a phase shifter. The mixer output was then viewed on an oscilloscope, where we could see the envelope of each pulse as well as the echo response from the signal.

The setup just described worked well for performing conventional two pulse spin-echo experiments, but some experiments required flexible control over several parameters including number of pulses and relative phase between pulses, which this switch-based setup could not provide. To address this need, we used an AWG manufactured by Tabor Electronics, which allows for precise control of the amplitude, frequency and phase of two RF outputs. These outputs could be controlled by creating a digital waveform for each channel and downloading these waveforms onto the AWG. In this way we generated a $\sim$4 GHz CW output on one channel (the reference) while generating a pulsed output at the same frequency on the other channel (the source). In principle,

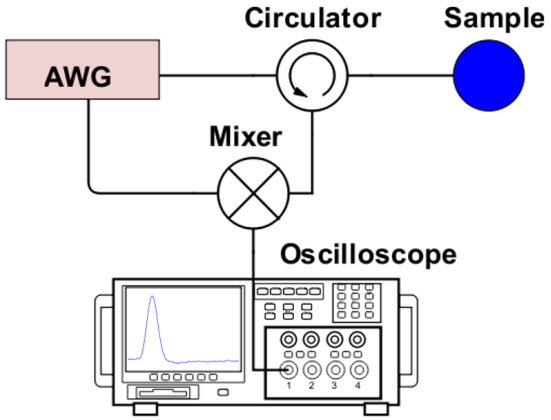

Figure 3.4: Block diagram of the essential components in our circuit. Amplifiers, attenuators and filters are not shown, but see Figure 3.3.

the ability to generate pulse patterns directly from the source output would remove the necessity of using hardware switches, but in practice we found that the AWG put out "noise" at the frequency of the device's sample clock, which obscured our experimental signal unless we applied additional gating to the output using the switches. Thus we retained most of the hardware from the original setup and continued to use the FPGA for timing control, including to trigger the AWG.

It is worthwhile to describe some practical aspects of the AWG's operation since this placed some important constraints on the flexibility of our setup. To generate a digital sine wave output, one must specify the vertical position of points on the sine curve at regularly spaced time intervals, and the timebase resolution of any digital signal is specified by the sample frequency f_s, which is the inverse of the time between consecutive points T:

$$f_s = \frac{1}{T}. \tag{3.1}$$

According to the Nyquist-Shannon sampling theorem, a signal with no frequency components higher than f_{max} can be fully determined by a digital waveform with sample frequency $f_s = 2f_{max}$ [28], so in general it is desirable to have a sample frequency at least twice the highest desired signal frequency. However, there are some techniques one can utilize to get around this minimum sample frequency requirement. Given a sample frequency f_s, we refer to the range of frequencies $\frac{1}{2}(n-1)f_s < f < \frac{1}{2}(2n-1)f_s$ as the nth Nyquist zone ($n \geq 1$), and it is well known that a digital waveform of frequency $f_o < \frac{f_s}{2}$ will also produce a signal in each higher Nyquist zone. These other signals will have frequencies given by

$$f_{N,\pm} = Nf_s \pm f_o, \tag{3.2}$$

for $N \geq 1$, as shown in Figure 3.5. Note that in this notation, frequencies in odd-numbered Nyquist zones will be written $f_{N,-}$ for some N, and those in even-numbered Nyquist zones will be written $f_{N,+}$.

We can thus in principle generate a sine wave at any desired frequency f by choosing a convenient sample frequency and then calculating the first Nyquist zone equivalent frequency of f. As an example, let's suppose we choose a sample frequency f_s and want to produce a frequency f in the second Nyquist zone (N=1). From equation 3.2 and the comment following it, we know we can write $f = f_s - f_o$, for some frequency $f_0 < f_s/2$. Then if we set the frequency of our digital signal to be $f_0 = f_s - f$, we know we will get the

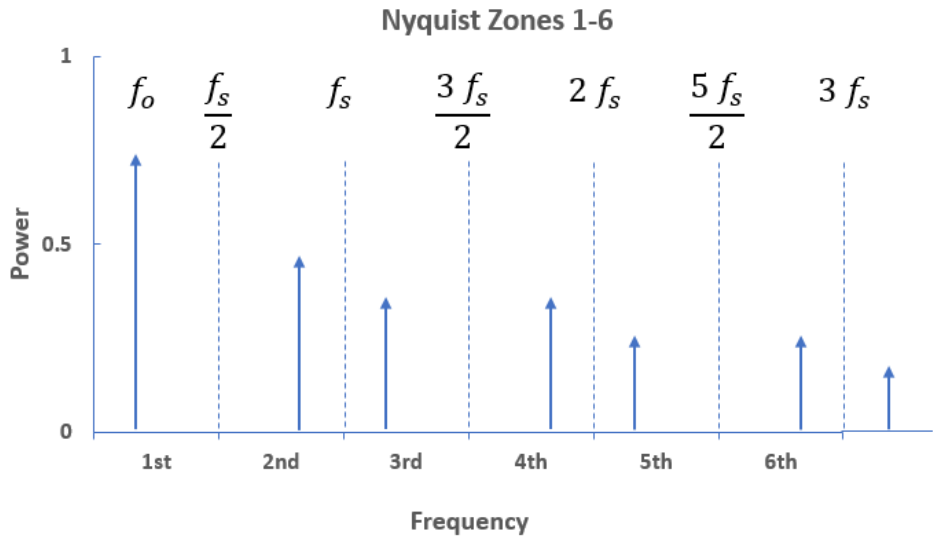

Figure 3.5: Diagram of the first six Nyquist zones for sample frequency f_s. A digital signal with frequency f_o will also produce signals in each higher Nyquist zone, with frequencies given by equation 3.2. However, frequencies in higher Nyquist zones than one will generally have reduced power.

desired frequency f as one of the output frequencies. We can even ensure that f is the only frequency that reaches our sample by applying a bandpass filter to the AWG output that is sharply centered on f, thus removing all other frequency components. In practice, however, all frequency components in Nyquist zones higher than the first will have reduced amplitude, and it may simply not be possible to get enough power in higher Nyquist zones to make this approach viable.

The Tabor AWG we used has a maximum sample frequency of 6 GHz (and only up to 5 GHz in some modes), but it is equipped with four different sampling modes, which can be used to maximize the output signal in Nyquist zones 1, 2, 3 or 4. Each sampling mode specifies a slightly different method for obtaining an analog output signal from a digital waveform, and we found that by using the RF sampling mode we were able to get an acceptable signal in the second Nyquist zone with a sample frequency of 5 GHz. As described above, we could then obtain a 4.2 GHz output signal (for instance) by setting the AWG to produce a 800 MHz signal and filtering out the components in every Nyquist zone but the second. In this way we were able to produce the desired $\sim$4 GHz outputs on the two AWG channels, using the CW channel as a mixer reference and the pulsed channel to probe the sample.

There are some disadvantages to this approach in general. Firstly, with a maximum sample frequency of only 6 GHz, it may not be possible to generate sufficient power at frequencies much higher than 5.5 GHz, which may be desired for future experiments on different samples. Secondly, because there are many frequency components present other than the desired frequency, it

is necessary to filter the AWG outputs. Finally, as already mentioned, with our AWG there is some ever-present "noise" at the sample clock frequency included in the output, which must be blocked with a manual switch unless it is far enough from the desired output frequency to be filtered out.

The use of an AWG allows exquisite control over parameters such as power, frequency, and phase of the signal produced and allows us to create intricate pulse sequences with large numbers of pulses. All of these properties are of great utility to us in designing our experiments, as described in the remainder of this chapter.

3.3 Spin Echo

We have already described how our ESR spectrometer allows us to probe our sample with complex RF pulse sequences and to observe the response on an oscilloscope. In this section we will describe why these pulse sequences are useful to us in probing properties of the sample.

The physical phenomenon known as spin echo was first discovered in Nuclear Magnetic Resonance experiments in 1950 by Erwin Hahn [29]. In NMR experiments it is nuclear spins that are manipulated to produce an echo signal while in ESR experiments an exactly analogous process occurs with spins of unpaired electrons.

As described in chapter 2, we can visualize the state of each electron spin as an arrow on the 3-dimensional Bloch sphere, and we can perform arbitrary rotations of these spins by applying an RF oscillating transverse magnetic field

to the sample. For spin echo, we start by assuming that the system has been prepared so that the majority of spins are in a given state, say the $|+\rangle$ state, and we can choose the vertical axis to point parallel to $|+\rangle$ (Figure 3.6 (a)). We showed in chapter 2 that in the absence of an external magnetic field, $|+\rangle$ is an eigenstate of the molecule's Hamiltonian and each spin will precess about the z axis of the Bloch sphere with some frequency ω_0.

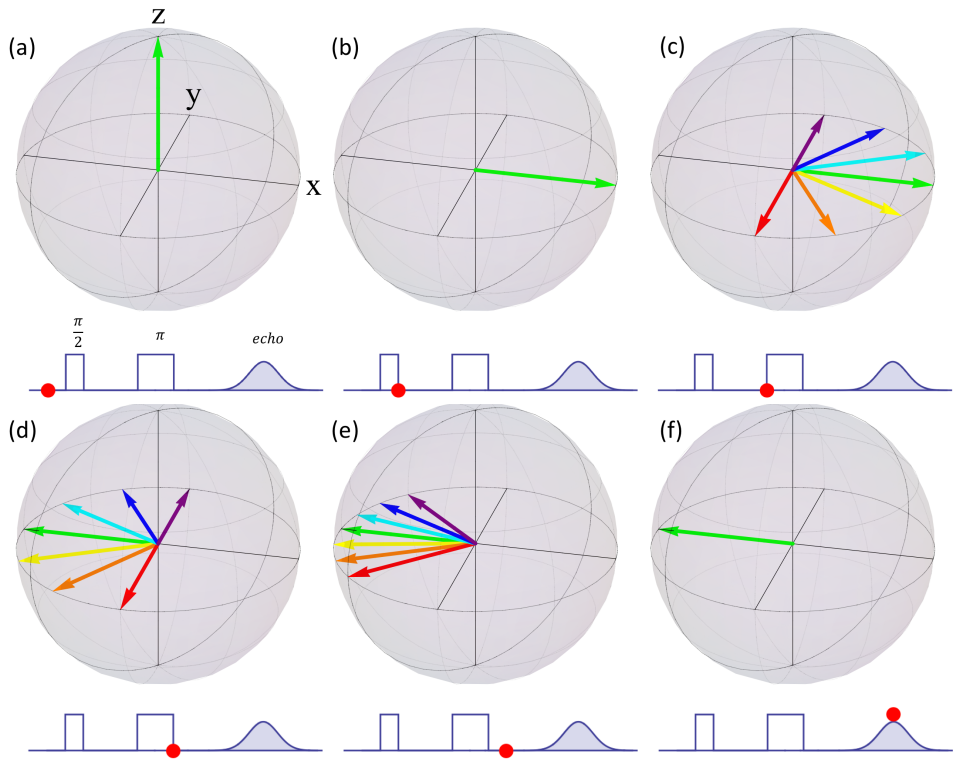

Figure 3.6: The dynamics of a collection of spins in a spin-echo experiment by visualizing spins as arrows on a Bloch sphere, as seen from a reference frame precessing about the z axis with the same frequency as the average spin. Initially all spins are aligned with the z axis (a) and a pulse is applied to rotate them onto the x axis (b). The spins then dephase for a time τ (c) before a refocusing π pulse is applied to flip all spins about the y axis by 180° (d). After this second pulse the spins continue rotating relative to our reference frame (e) and rephase with each other at a time 2τ after the initial pulse, at which time they all align along the -x axis (f).

We then apply an oscillating magnetic field for an appropriate duration to rotate the spins by an angle $\frac{\pi}{2}$ about an axis in the horizontal plane of the Bloch sphere, so that after the pulse they end up pointing along another horizontal axis, say the x axis (Figure 3.6 (b)). As shown in chapter 2, we want to choose the frequency ω of the oscillating magnetic field to be close to ω_0 so as to drive oscillations between the $|+\rangle$ and $|-\rangle$ states. After the rotation has been applied, each spin will then continue to precess about the z axis of the Bloch sphere in the x-y plane. The spin-echo phenomenon is easiest to analyze if we work in a reference frame rotating at frequency ω along with these precessing spins.

Now if every spin precessed at exactly the same rate $\omega_0 = \omega$, they would all rotate along with our reference frame and thus would remain aligned with the x axis indefinitely. However, there will be small differences in the energy splitting $2E$ between the $|+\rangle$ and $|-\rangle$ states for different spins and additionally each individual spin will create a small magnetic field of its own so that the actual local magnetic field in the vicinity of each spin will be slightly different from the externally applied field. These two factors will cause the Hamiltonian seen by each spin to be slightly different and hence each spin will precess at a slightly different frequency. As viewed from our rotating frame, then, each spin will slowly rotate away from the x axis, each precessing at its own frequency $\omega_0 - \omega$ (Figure 3.6 (c)). This process in which the spins effectively spread out away from the x axis is referred to as dephasing.

If we allow the spins in our system to dephase for long enough, they will eventually be randomly distributed in the x-y plane, but by applying a second

RF pulse to the sample we can cause the spins to refocus along a single axis at some later time. Having waited some time τ after the first pulse, we apply a second RF pulse identical to the first except with twice the duration, causing each spin to rotate through an angle π about the y axis. As shown in Figure 3.6 (d), this will have the effect of reversing the x component of each spin vector on the Bloch sphere. Subsequently, each spin will continue to rotate in the x-y plane relative to the x axis of our reference frame, but this rotation will now cause all spins to rotate toward the negative x axis, as shown in Figure 3.6 (e). Moreover, those spins that are rotating faster in our frame will have traveled through a larger angle during the time τ between pulses. Once flipped by the second pulse, these faster spins will therefore have to travel through a larger angle to reach the -x axis than spins rotating more slowly. The result is that at a time τ after the second pulse, all spins will reach the -x axis simultaneously, as shown in Figure 3.6 (f).

Once all spins have rephased along the -x axis, they will create a net magnetic moment and thus induce a net magnetic field in the vicinity of the sample in addition to the externally applied field. The change in magnetic field produced by the refocused spins precessing in the lab frame induces a voltage signal, which we can measure with an oscilloscope. We refer to the signal created in this way as an echo and to an experiment using this physical process as a spin-echo experiment.

In this description of the spin-echo phenomenon we have made a number of assumptions that will not hold perfectly in a realistic experiment. For example, we assumed that no dephasing occurs during the pulses themselves,

which is clearly not exactly true. In practice, we try to make our pulses short so as to approach the ideal limit described here, but it is important to be aware of whether this assumption is a good approximation of reality. Further, we assumed that the precession frequency of any given spin does not change appreciably over the course of the experiment so that each spin will rotate away from the x axis with a constant angular frequency. In practice, of course, the precession frequency of each spin will change in time. This is important because if spins in the sample are rotating at different frequencies before and after the π pulse is applied, then they will not rephase on the -x axis. This particular aspect of spin echo is central to my measurements, as discussed in the next section.

3.4 Decoherence

Now that we have described the principle of spin echo and the specific pulse sequences used to observe spin echo in our system, we can describe the measurements we made using these techniques. As described in section 3.3, the echo signal results when spins that have been rotated into the x-y plane are allowed to dephase for a time τ before being refocused by a π pulse. Recall that the dephasing occurs because each spin is precessing about the z axis at a slightly different angular frequency, due to each molecule experiencing a slightly different local magnetic field and/or slight differences between molecules in the energy splitting $2E$ between the $|+\rangle$ and $|-\rangle$ states.

In our previous discussion, we assumed that the precession frequency of

each individual spin was approximately constant for the duration of their evolution, in which case all spins will rephase simultaneously on the -x axis at a time τ after the π pulse. In reality, however, neither the local magnetic field nor the energy splitting $2E$ will be exactly constant in time for individual molecules. Therefore each spin will generally have a different average rotation frequency ω_0 before and after the π pulse. The result is that this particular spin will have to traverse a larger angle than average to reach the -x axis and will also be rotating more slowly, with the consequence that it will reach the -x axis later than time τ after the π pulse (Figure 3.7).

Thus in reality not all spins will reach the axis simultaneously, and this will reduce the net magnetic field produced by the refocused spins and hence also the induced voltage signal we measure. Therefore the more dynamical variation there is in local magnetic field and E for individual molecules during the evolution time $t = 2\tau$, the smaller the echo signal will be. This phenomenon in which we become unable to rephase spins in the sample as a result of interaction with the spins' environment is called decoherence. In the presence of decoherence, we expect the echo size A to decay exponentially with evolution time t, according to

$$A = A_0 e^{-t/T_2}, \tag{3.3}$$

where $A_0 = A(0)$ is the initial amplitude and T_2 is the coherence time introduced in chapter 1. We now see that T_2 is simply a constant measuring the rate of decoherence in the sample. Therefore we can measure the coherence time for a sample by conducting spin-echo experiments with a range of delay times τ, measuring the size of the echo for each experiment and then fitting

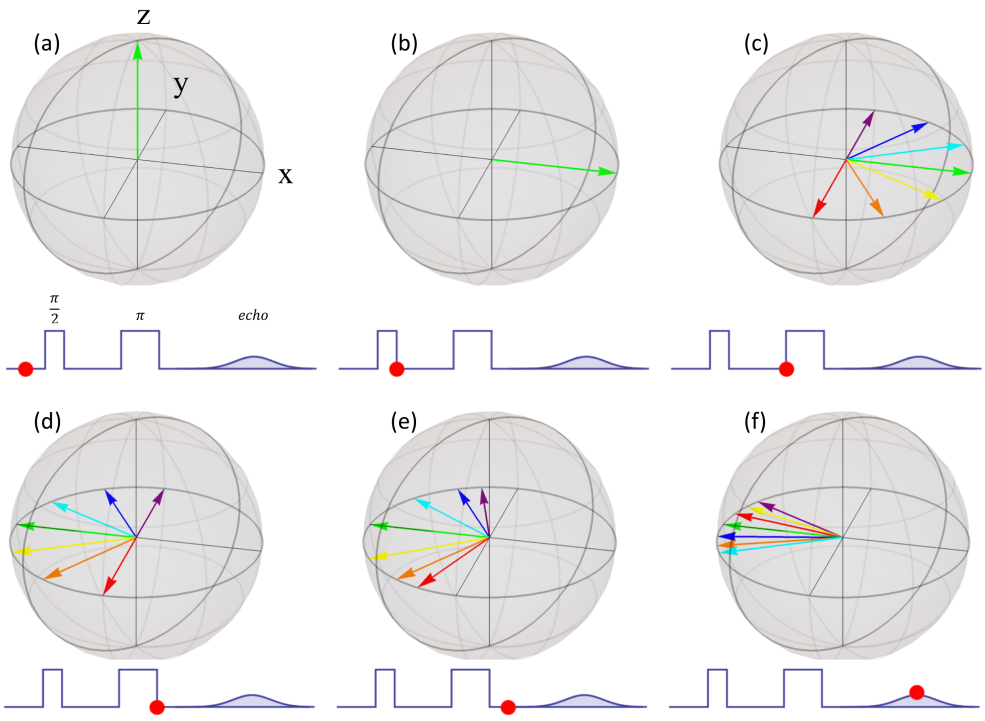

Figure 3.7: Dynamics of a collection of spins in a spin-echo experiment accounting for decoherence, as seen from a reference frame precessing about the z axis with the same frequency as the average spin. Initially all spins are aligned with the z axis (a) and a pulse is applied to rotate them onto the x axis (b). The spins then dephase for a time τ (c) before a refocusing π pulse is applied to flip all spins about the y axis by 180° (d). After this second pulse the spins continue rotating relative to our reference frame (e), but due to decoherence they do not rephase perfectly (f).

the graph of echo size versus evolution time to a decaying exponential, with T_2 as a fit parameter.

Now suppose we want to observe Rabi oscillations in our system (see section 2.2). We can do this by using a three-pulse sequence in which the first pulse rotates the spins about the y axis of the Bloch sphere by some variable angle ϕ_0. As we increase the angle ϕ_0, the echo amplitude will oscillate sinusoidally

with frequency ω_R, as given by equation 2.31. Figure 3.8 shows how this works for the angle $\phi_0 = \pi$. Note that the wait time between the initial and $\pi/2$ pulses should be longer than T_2, so that the components of the spins in the x-y plane of the Bloch sphere will be randomly distributed by the time the $\pi/2$ pulse is applied. The situation considered in chapter 2 assumed no decoherence, but we have just shown that the effect of decoherence will be to reduce the signal amplitude as given by equation 3.4. Thus in an actual Rabi oscillation experiment with decoherence, we expect the signal size for pulse length t to be

$$Y = A_0 e^{-t/T_{Rabi}}(1 + \cos(\omega_R t)), \tag{3.4}$$

where T_{Rabi} is the time constant of the decay and A_0 is a constant. We will see how we can use this equation to fit actual Rabi oscillation data in the next two chapters.

3.5 Carr-Purcell-Meiboom-Gill

In the experiment described in the previous section, we increase the delay time between the $\pi/2$ and π pulses and thus increase the evolution time $t = 2\tau$ over which decoherence occurs in the sample. However, by applying a sequence of more than two pulses it is often possible to maintain coherence in the sample for longer evolution times. In general, there may be multiple processes causing decoherence and each process may have a different characteristic timescale over which it works. Suppose, for example, that there are two mechanisms M_1 and M_2 causing the spins' precession frequencies to vary, and that these occur at

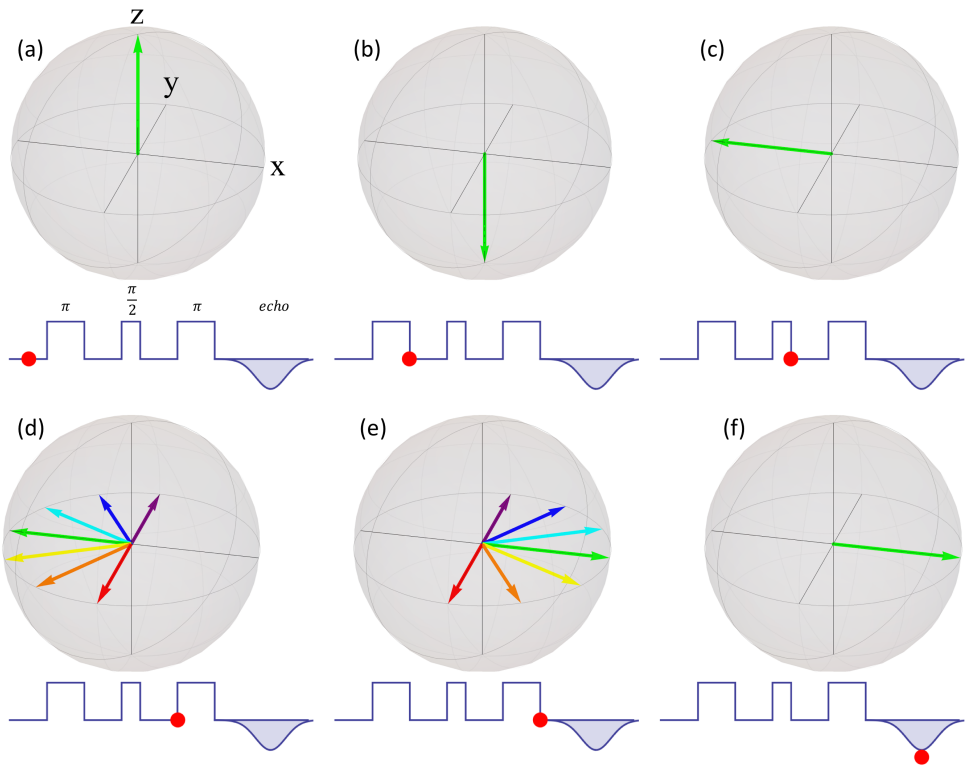

Figure 3.8: A spin-echo experiment represented with Bloch spheres, with an initial π pulse added, as seen from a reference frame precessing about the z axis with the same frequency as the average spin. Initially all spins are aligned with the z axis (a) and a pulse is applied to rotate them onto the -z axis (b). After a time $t_0 > T_2$, a $\pi/2$ pulse is applied to rotate the spins to the -x axis (c). The spins then dephase for a time τ (d) before a refocusing π pulse is applied to flip all spins about the y axis by 180° (e). After this third pulse the spins continue rotating relative to our reference frame and rephase with each other at a time 2τ after the $\pi/2$ pulse, at which time they all align along the x axis (f). (Note: pulse timing is not to scale.)

rates Γ_1 and Γ_2, respectively, with $\Gamma_2 > \Gamma_1$.

Now let us apply a pulse sequence to our sample that consists of one $\pi/2$ pulse and N π pulses, all about the same axis, as shown in Figure 3.9. Let us fix a time τ between the $\pi/2$ pulse and the first π pulse and make the time between successive π pulses equal to 2τ. Let's suppose that we have chosen

τ so that $\Gamma_1 < 1/\tau < \Gamma_2$. Then between the $\pi/2$ and π pulses, many spins will change precession frequency due to process M_2 but only a few will be affected by process M_1. Then the π pulse will refocus the spins and they will be (mostly) rephased at time τ after the π pulse. They will then dephase again for time τ before the next π pulse refocuses them, and again there will be decoherence due to process M_2 but not much due to M_1. The experiment will continue in this way for each successive pulse, with the effect that process M_2 will contribute almost as much to the spins' decoherence as without the extra pulses, whereas process M_1 will not contribute much. As a result, any decoherence that was due to process M_1 will be mitigated relative to a two-pulse sequences with the same evolution time.

Of course, this result is only true provided $1/\Gamma_1$ is not longer than the total evolution time in the experiment, t_{total}. Otherwise, the two-pulse and N-pulse experiments will be equivalent since the effects of process M_1 will be removed by either sequence. Therefore we conclude that using a sequence of N π pulses instead of just one will mitigate the effects of decoherence processes that occur at rates roughly satisfying

$$1/t_{total} < \Gamma_1 < 1/\tau. \tag{3.5}$$

In this discussion we assumed that the experiment is designed so that each π pulse rotates the spins about the same axis as the $\pi/2$ pulse and in the same direction, and such a sequence is referred to as a Carr-Purcell pulse sequence. However, we can sometimes achieve even better results with slight variations

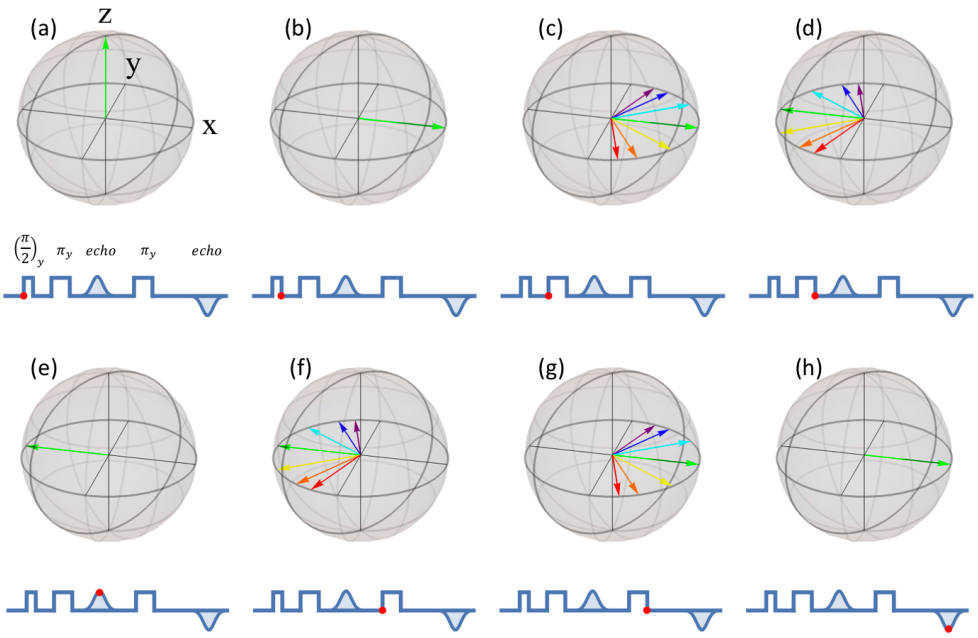

Figure 3.9: A Carr-Purcell experiment with just two π pulses, as seen from a reference frame precessing about the z axis with the same frequency as the average spin. Initially all spins are aligned with the z axis (a) and a $\pi/2$ pulse is applied to rotate them onto the x axis (b). The spins then dephase for a time τ (c) before a refocusing π pulse is applied to flip all spins about the y axis by 180° (d). After this pulse the spins continue rotating relative to our reference frame and rephase with each other at a time τ after the π pulse, at which time they all align along the -x axis (e). The spins then begin dephasing again (f) and are again refocused by a π pulse about the y axis (g). Subsequently the spins rephase along the x axis and produce an echo (h).

of this model. In particular, we could have had each π pulse rotate the spins about the x axis rather than the y axis (Figure 3.10). It is that particular pulse sequence that is referred to as a Carr-Purcell-Meiboom-Gill (CPMG) sequence. The CPMG sequence has the advantage that it protects somewhat against imperfections in pulse length since the $\pi/2$ and π pulses are not along the same axes. In our experiments we used a standard CPMG pulse sequence.

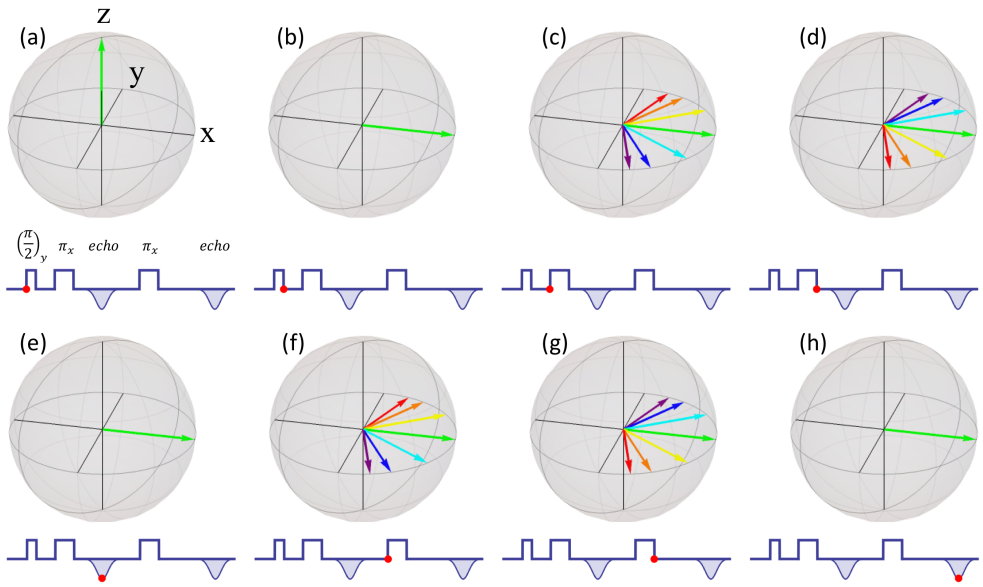

Figure 3.10: A CPMG experiment with two π pulses that rotate spins about the y axis, as seen from a reference frame precessing about the z axis with the same frequency as the average spin. Initially all spins are aligned with the z axis (a) and a $\pi/2$ pulse is applied to rotate them onto the x axis (b). The spins then dephase for a time τ (c) before a refocusing π pulse is applied to flip all spins about the x axis by 180° (d). After this pulse the spins continue rotating relative to our reference frame and rephase with each other at a time τ after the π pulse, at which time they all align along the x axis (e). The spins then begin dephasing again (f) and are again refocused by a π pulse about the x axis (g). Subsequently the spins rephase along the x axis and produce an echo (h).

We have shown that CPMG sequences will mitigate the effects of a certain subset of decoherence process, namely those with characteristic rates Γ_1 satisfying equation 3.5. In general, the total decoherence rate Γ due to multiple processes $M_1, ..., M_n$ will be the sum of the individual rates:

$$\Gamma = \Sigma_{i=1}^{n} \Gamma_i. \tag{3.6}$$

So if we can use a CPMG pulse sequence to reduce the effects of some of these processes, this will reduce the overall decoherence rate in our system, and therefore increase the coherence time $T_2 = 1/\Gamma$.

Chapter 4

Methods

All experiments described in this thesis were conducted by loading a dilute liquid Cr_7Mn sample into a loop-gap resonator, cooling the sample and resonator in the PPMS cryostat and applying RF pulses at the resonant frequency of the resonator to perform spin-echo experiments on our sample. In this chapter we describe our sample preparation and mounting methods, details of our loop-gap resonators and our procedure for background subtraction. We also describe how we used spin-echo experiments to measure coherence times in our samples and to observe Rabi oscillations, which allowed us to measure the amplitude of the RF oscillating field in our resonator.

4.1 Sample Preparation

The Cr_7Mn samples used in our experiments were synthesized by the group of Richard Winpenny in the School of Chemistry at University of Manchester and shipped to us in a powder form. To prepare dilute liquid samples, we measured

out a fixed quantity of Cr_7Mn by weight and calculated an appropriate volume of toluene or benzene solvent to achieve the desired sample concentration (see Appendix A for a sample calculation). After dissolving the Cr_7Mn powder in our solvent, we used a syringe and needle to inject a small quantity of solution into a quartz capillary tubes of about 6 cm in length and 0.5 mm in inner diameter, which we had sealed at one end ahead of time by heating with a micro torch. After injecting the solution we sealed the other end of each tube, being careful that the solution had accumulated at the far end of the tube from the torch. After sealing, we could redistribute the solution within the tube by shaking it, which was often necessary to ensure that the volume of solution in the loop of our resonators was not larger than the resonator volume. It was desirable to have a sample volume not too large so that the RF oscillating magnetic field in the resonator was roughly constant over the sample volume. A typical sample in its capillary tube is shown in Figure 4.1 along with a loop-gap resonator (see section 4.2). The green color is characteristic of the particular variant of Cr_7Mn used in our experiments; because toluene is colorless, more dilute samples can be distinguished to some degree by their lighter color.

4.2 Loop-Gap Resonators and Sample Mounting

We described in chapter 3 how we can generate a pulsed RF signal using an AWG or other signal source but we need to transmit this signal to the sample

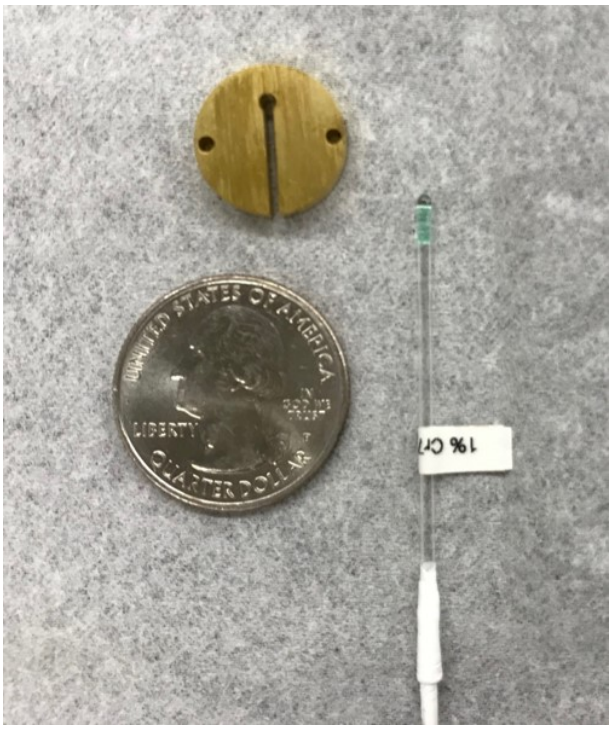

Figure 4.1: A 1% Cr_7Mn sample (green) diluted in toluene in a capillary tube along with a loop-gap resonator with resonant frequency about 4.9 GHz.

in the form of an RF oscillating magnetic field at the sample location. We use a coaxial cable to direct the signal down into the cryostat to the bottom of the probe, where the coaxial cable terminates in an antenna inside a copper shield.

We place a loop-gap resonator (Figure 4.1) inside the shield just below the antenna. When a pulse of RF radiation reaches the antenna, the antenna will radiate and create oscillating electric and magnetic fields inside the shield. If the frequency of radiation is close to the resonant frequency of the resonator (usually within a few MHz, depending on the resonator's quality factor, Q, as described below), then the resonator will absorb the radiation and concentrate

the oscillating magnetic field in the resonator's loop and the electric field in the gap. This gives us a way to create an oscillating magnetic field that is relatively uniform over the volume of the resonator loop. Figure 4.2 shows the amplitude of reflected radiation from the resonator as the frequency of input radiation is swept over a range of 200 MHz, measured using a Vector Network Analyzer. The dip in reflection corresponds to the resonant frequency of the resonator where radiation is strongly absorbed.

We used a number of loop-gap resonators with slightly different properties in our experiments and also varied properties of each resonator in two ways (for more details on loop-gap resonators see [30]). The most important properties of the resonators for our purposes were their resonant frequency, quality factor (Q) and thickness. In general, thicker resonators will give a more uniform RF magnetic field over a larger volume than will smaller resonators, since a larger volume of the loop is far from the boundary.

The resonant frequency of the resonator is important because it will only absorb radiation strongly at that frequency. In order to generate an RF field that will drive transitions between the $|+\rangle$ and $|-\rangle$ states of our sample we needed the resonator's frequency to be close to the transition frequency between these states. Therefore we wanted a resonator with frequency around 4 GHz. Fortunately, even after fabrication we can easily decrease any resonator's frequency by a variable amount up to roughly 1 GHz by inserting a small slab of sapphire (dielectric constant $\sim$10) into the resonator's gap. Using this technique, we performed spin-echo measurements on our samples over a wide range of frequencies ($\sim$ 3.8 to 4.8 GHz).

Finally, the Q of a resonator is related to the resonator's center frequency f_c and bandwidth Δf by $Q = f_c/\Delta f$, and is important because it determines both the bandwidth of frequencies that will be absorbed and the time scale over which energy will be dissipated from the resonator. A resonator that has a high Q value will take a long time to dissipate absorbed energy, which can be problematic because it distorts the short ($\sim$100 ns) pulses put into the resonator, as well as the signal we want to measure. To prevent excessive distortion we generally tried to keep the Q value below about 200, which we achieved by placing a small piece of absorbing material near the end of the resonator's gap. The absorbing material used is Eccosorb QR13 absorber manufactured by Emerson and Cummings Microwave Products. We could also adjust the Q value by changing the coupling between resonator and antenna, which was achieved by changing the relative orientation of the two until we found a good coupling.

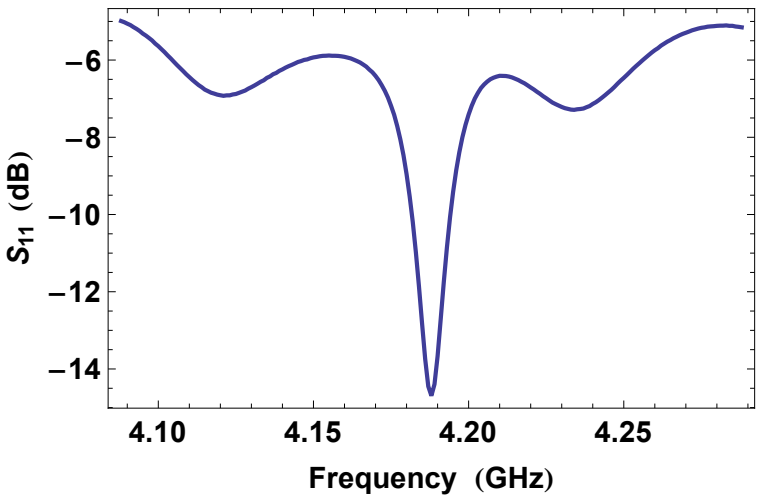

Figure 4.2: Log magnitude of reflected radiation as the input frequency is swept over a range of 200 MHz. The peak in the center corresponds to a resonant frequency of the resonator, which we see is about 4.19 GHz.

For all our experiments, we want the sample to sit exactly inside the resonator loop so as to get a strong, uniform magnetic field over the volume of the sample. To do this, we made a small hole in the bottom of the shield and for each sample we put just enough teflon tape on the outside of the sample tube on the end away from the sample (Figure 4.1) so that it fits snuggly in this hole. We then insert the sample tube through the hole so that the sample sits in the resonator loop, as shown in Figure 4.3. The tape wrapped around the bottom of the tube is generally sufficient to prevent the sample tube from moving as long as we load the probe into the resonator with some care.

After loading our sample into the resonator inside the shield, we attached the shield to the SMA connections at the bottom of our probe and loaded the probe into the PPMS cryostat, which we used to cool the sample to temperatures ranging from 1.8 K to almost 10 K. Once the desired temperature was reached, we used the VNA to find the resonant frequency of the resonator at that temperature and set the signal source or AWG to generate pulse sequences at that frequency, which we used to probe the sample through spin-echo measurements, as described in section 4.4.

4.3 Background Subtraction

As described in chapter 3, the signal we want to measure can be observed as a brief change in voltage (an "echo") and displayed on an oscilloscope screen. The echo resulting from a single $\pi/2 - \pi$ pulse sequence is tiny compared to the noise and background signal in our experiment. By running the pulse

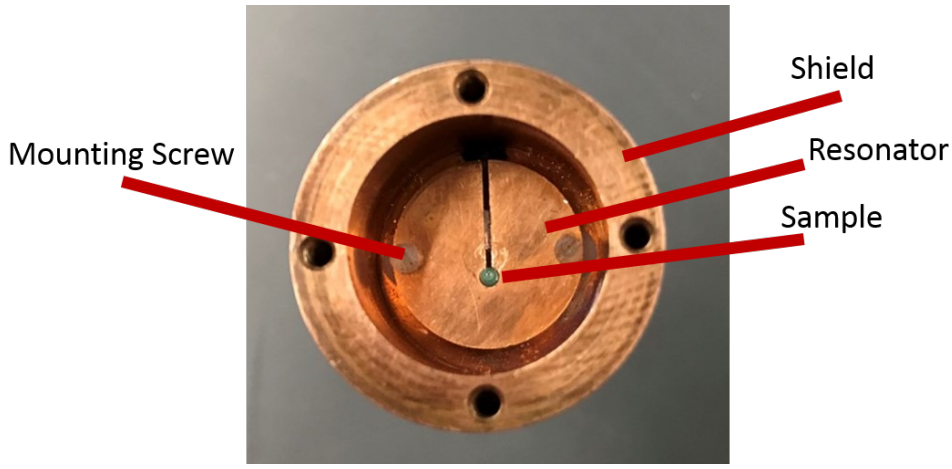

Figure 4.3: Photograph of a Cr_7Mn sample mounted inside the loop of a resonator inside a shield.

sequence many times and setting the oscilloscope to average over a large number of measurements, we can see an echo on the oscilloscope screen under ideal conditions, that is, when the echo is at its largest. However, even with this averaging the echo is relatively small compared to the background and to measure smaller signals it is essential to use some background subtraction procedure.

To improve the signal-to-background ratio in our experiment we came up with a background subtraction algorithm based on the properties of spin echoes discussed in chapter 3. As described in that chapter, the amplitude and phase of the echo signal coming from our sample will depend on the orientation of the sample's spins on the Bloch sphere at the time of the echo. Specifically, let us fix the z axis to be parallel to the state $|+\rangle$ (the vertical axis of the Bloch sphere) and choose the x axis to be the axis aligned with the sample spins' state after they have been rotated by a $\pi/2$ pulse that is in-phase with

the AWG reference output. Then we know from section 2.2 that if the spins are precessing together in the x-y plane of the Bloch sphere, they will induce a current in a nearby antenna. Moreover, the phase of the induced signal will depend on the spin's angle about the z axis.

Recall that the signal coming from the sample is mixed with the reference signal from the AWG in an IQ mixer. The I (in-phase) channel of the mixer will output the component of the sample signal that is in-phase with the reference, while the Q (quadrature) channel will output the component that is 90° out of phase. If we view the output of the I channel on an oscilloscope, then, the amplitude of the signal will depend the relative phase of the two inputs, with the maximum amplitude occurring when the phase difference is zero. When the phase difference between the two inputs is 180° the signal in the I channel will again have the maximum amplitude but will be inverted relative to the signal with no phase difference. We already saw one way to obtain an inverted echo, by using a three-pulse sequence, in section 3.4 (see Figure 3.8). In our experiments we tuned the phase of the signal from the sample to get maximal signal amplitude in the I mixer output. Initially this was achieved by hand-tuning a phase-shifter placed in the circuit but after acquiring the AWG we were able to precisely control the relative phase of the pulsed and reference outputs.

The observations of the preceding two paragraphs show how we can subtract off systematic components of the background by running each experiment twice, with the signal from the sample having opposite phase in the two experiments. Assuming that the background does not depend on phase, then

adding 180° to the phase of the signal coming from the sample will reverse the sign of the echo signal coming from the I mixer output without changing the background at all. By subtracting the results of the two experiments from each other, then, we should be able to double the signal size while completely removing any component of the background that is systematic.

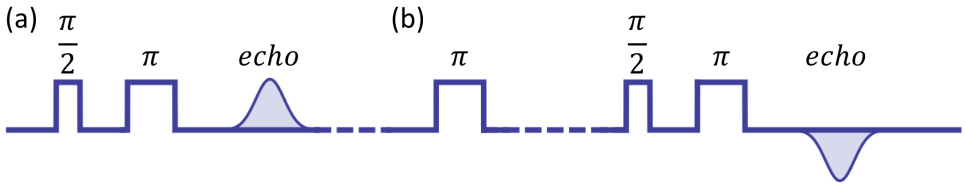

Figure 4.4: Schematic of the effect of alternating between a two-pulse and three-pulse sequence. Timing between pulses is not to scale.

To implement the background subtraction procedure described above, we used two different methods to reverse the phase of the signal coming from the sample. With our original signal source we could not control the phase of the pulses going to the sample, so instead we alternated the standard $\pi/2-\pi$ pulse sequence with a three pulse $\pi-\pi/2-\pi$ sequence (Figure 4.4). In this sequence, we always made the delay between the first π pulse and the $\pi/2$ pulse longer than T_2 so that the spins would have time to decohere before we applied the $\pi/2$ rotation. We refer to this extra pulse as a background subtraction pulse or "back-pulse". Bloch diagrams for this three-pulse sequences are shown in Figure 3.8. This should have the effect that after the $\pi/2$ pulse all spins are aligned along the -x axis rather than the x axis (Figure 3.8 (f)). As described above, this will reverse the phase of the signal from the sample, thus inverting the echo and allowing us to do the desired background subtraction.

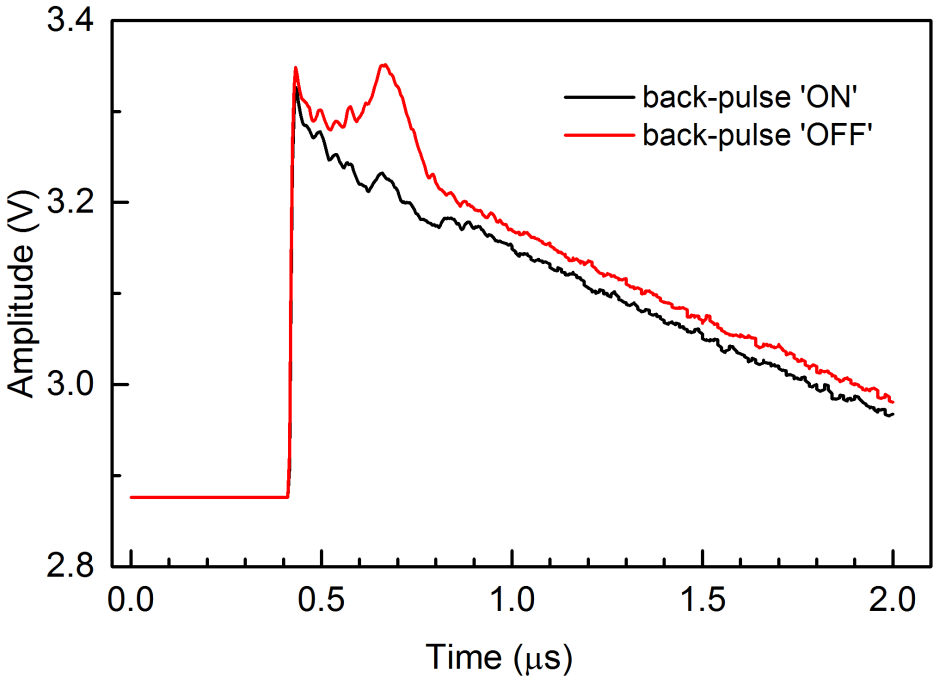

Figure 4.5: Oscilloscope traces showing the echo signal and a large background. We see that the echo from the three-pulse sequence (black) is much smaller than that from the two-pulse sequence (red).

In practice, we found that the echo size obtained using the back-pulse was significantly smaller than the two-pulse echo, as shown in Figure 4.5. This is not entirely surprising since we showed in section 3.4 that the amplitude of any echo signal will decrease with the length of the initial pulse (equation 3.3). This approach therefore only slightly increased signal size, but nonetheless it fulfilled the more important role of background subtraction. We refer to this method as the back-pulse method of background subtraction. An echo signal obtained using the back-pulse method is shown in Figure 4.6.

After acquiring the AWG we were able to precisely control the relative phase of the pulsed and reference output channels. Therefore we could easily

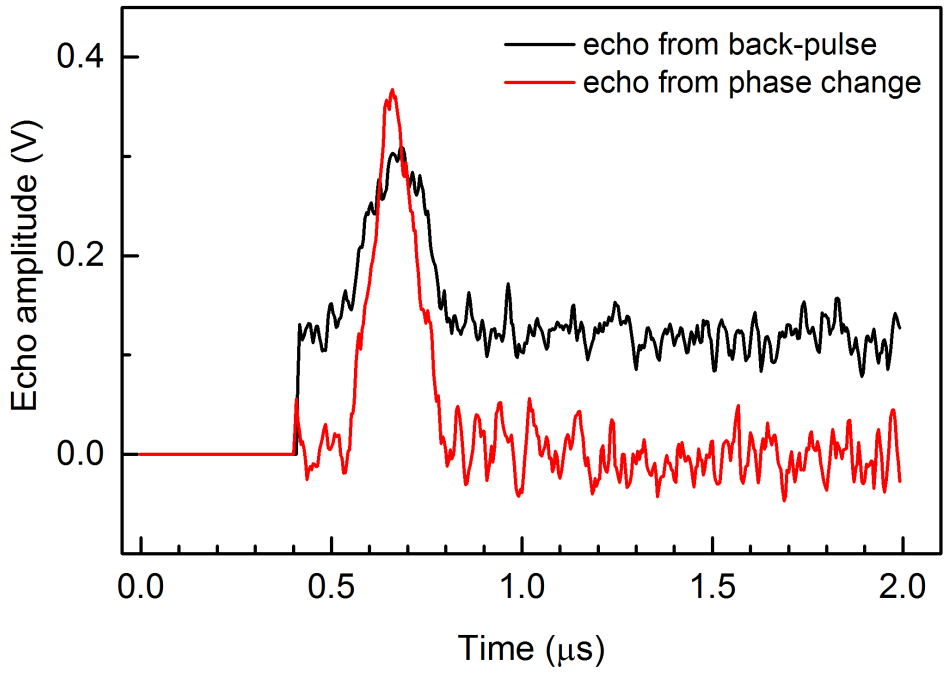

Figure 4.6: Echo signals after background subtraction, obtained by subtracting an inverted echo from an upright echo using two different methods. For the black trace, inversion was achieved by alternating a two-pulse and three-pulse sequence (back-pulse method, see Figure 4.4), while for the red trace it was achieved by changing the phase of the pulses in a two-pulse sequence (phase change method, see Figure 4.7). The phase change method is seen to give a larger signal size.

invert the echo signal by adding 180° to the phase of the pulsed channel while leaving the reference channel phase unchanged (Figure 4.7). Figure 4.8 shows oscilloscope traces taken with pulse sequences differing in phase by 180°. The background subtraction was then performed by subtracting signals generated from pulse sequences 180° out of phase with each other, and we found that this method both removed the background and doubled the signal size (Figure 4.6), as anticipated. We refer to this method as the phase-change method

of background subtraction.

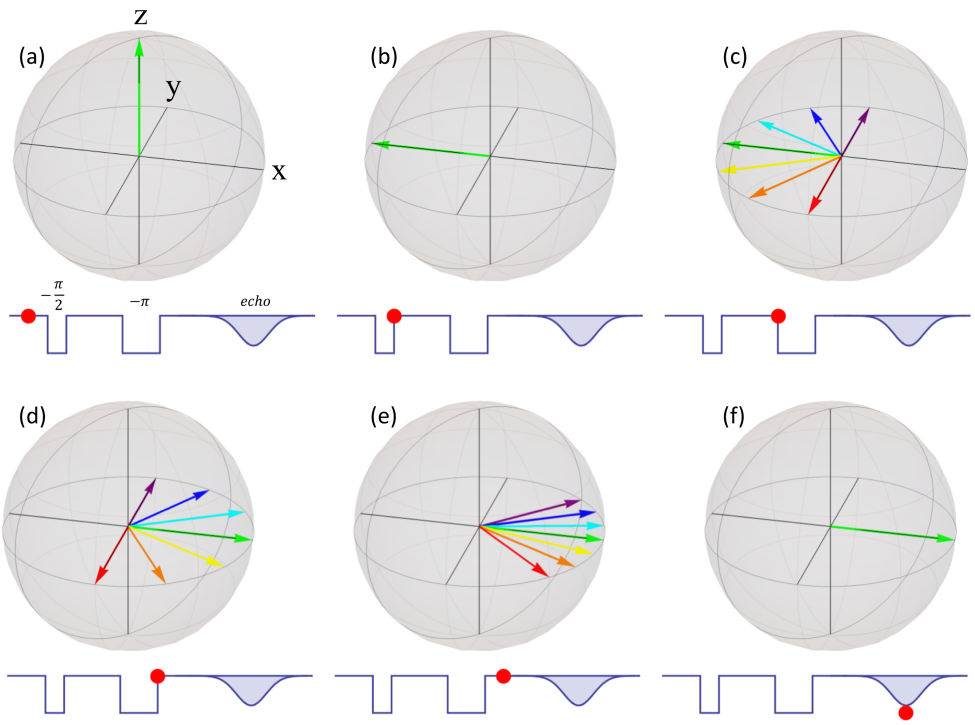

Figure 4.7: A spin echo experiment represented with Bloch spheres, with the phase of all pulses 180° off from the reference signal, as seen from a reference frame precessing about the z axis with the same frequency as the average spin. Initially all spins are aligned with the z axis (a) and a pulse is applied to rotate them onto the -x axis (b). The spins then dephase for a time τ (c) before a refocusing π pulse is applied to flip all spins about the y axis by 180° (d). After this second pulse the spins continue rotating relative to our reference frame (e) and rephase with each other at a time 2τ after the initial pulse, at which time they all align along the x axis (f). This results in an inverted echo relative to a pulse sequence in phase with the AWG reference channel.

4.4 Spin Echo Measurements

We discussed in chapter 3 how in a realistic spin-echo experiment, decoherence will prevent the π refocusing pulse from perfectly rephasing all spins after a

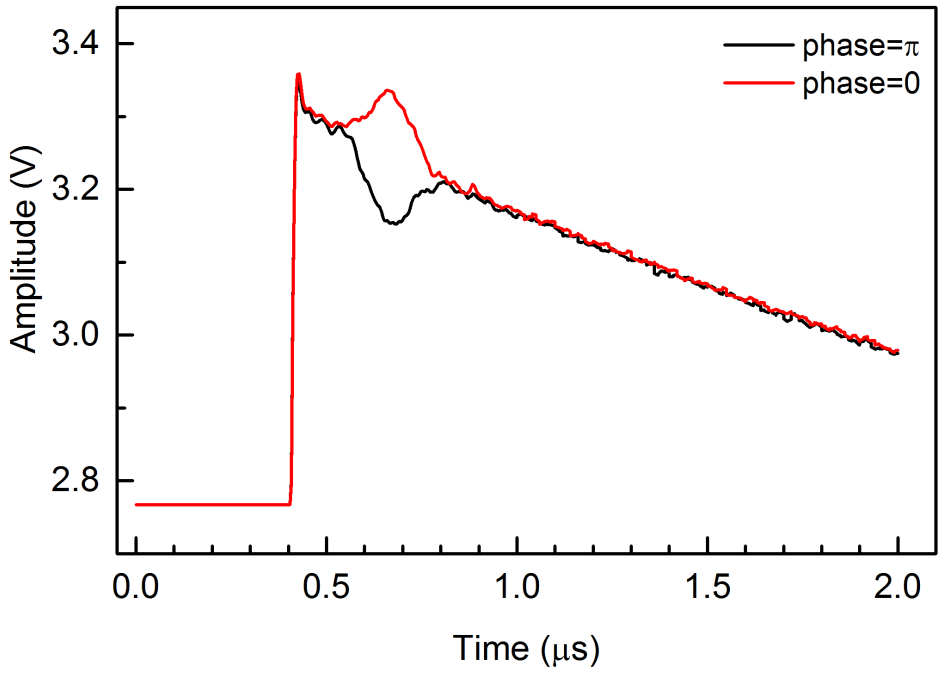

Figure 4.8: Oscilloscope traces showing the echo signal and a large background. The red and black traces were obtained using pulse sequences that were 180° out of phase with each other, causing the echo to be inverted.

period of dephasing. If this decoherence is truly random, then we expect the echo size A to decay exponentially with the evolution time $t = 2\tau$ according to the formula

$$A = A_0 e^{-t/T_2}, \tag{4.1}$$

where A_0 is a constant and T_2 is the coherence time. Figure 4.9 shows the result of a spin-echo experiment for a 1% Cr_7Mn sample diluted in toluene with a range of delay times τ between 0.25 μs and 1.25 μs.

We measured the coherence time by integrating the echo area for each experiment and then fitting the graph of echo area versus 2τ to a decaying

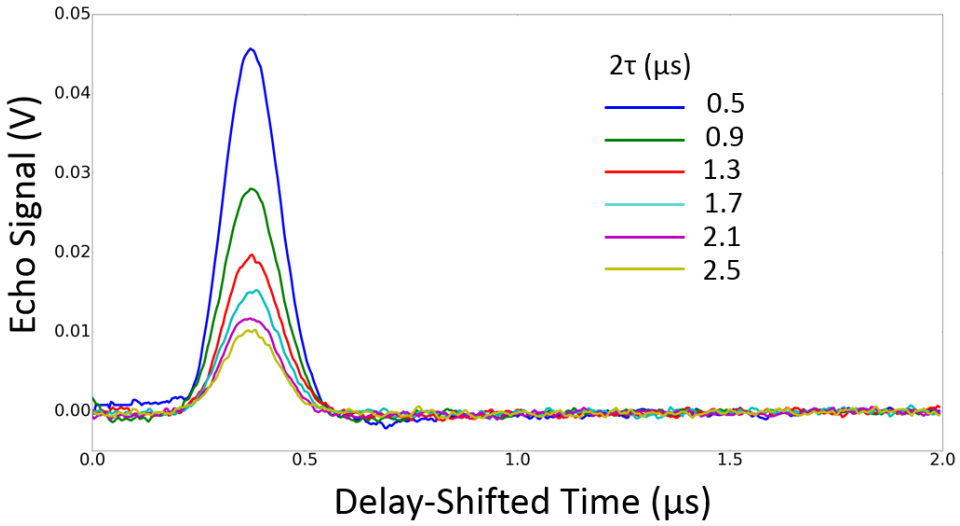

Figure 4.9: Echo signals measured from spin-echo experiments on a 1% Cr_7Mn sample in toluene for a range of delay times τ, with external magnetic field of 20 Oe and resonator frequency of 4.243 GHz. The length of the $\pi/2$ pulse was 50 ns. The horizontal axis for each trace has been shifted by the delay time in each case so that the echoes overlap.

exponential, with T_2 as a fit parameter. An example of such a fit is shown in Figure 4.10. Most of the results presented in chapter 5 were obtained by measuring T_2 in this way for a range of values of some parameter, such as magnetic field or temperature.

In all our experiments, there was a small remnant field in the magnet even when it was set to zero. Therefore, we identified the actual zero field by finding the field at which T_2 was maximum, since we expect T_2 to be peaked at zero field (see section 1.3). We then recorded the magnetic field value displayed at this peak and subtracted that value from all magnetic field values in our experiment. To confirm that the field we identified really was zero field, we set the magnet to produce negative fields and checked that there was no corresponding peak in T_2 at any negative field value.

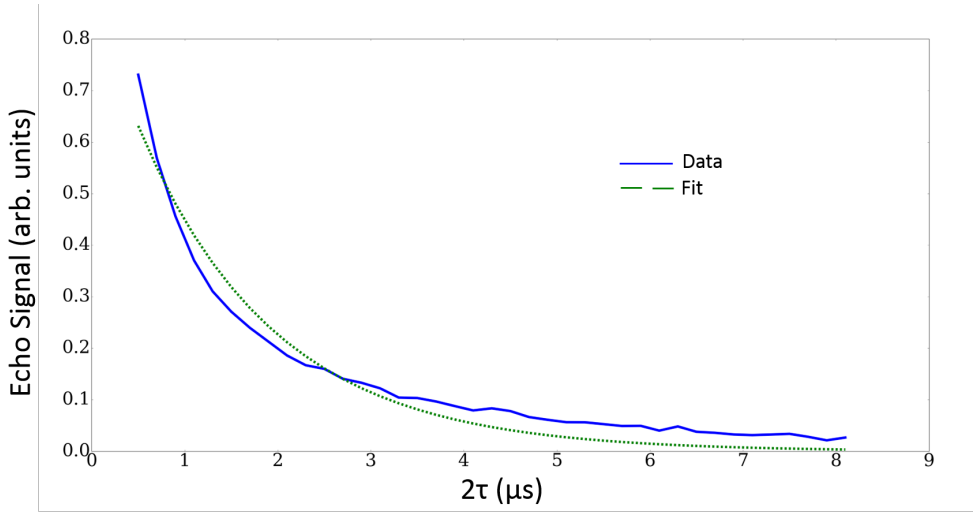

Figure 4.10: Integrated echo area versus 2τ for a 1% Cr_7Mn sample diluted in toluene along with a fit of the data to equation 4.1. The value of T_2 obtained from this fit was 1463 ± 77 ns.

We also wanted to measure the rate of decoherence in our samples when using the CPMG pulse sequences described in section 3.5, which we did in a very similar way to the measurements just described. Instead of varying the delay time between the $\pi/2$ and π pulses, we fixed a delay time between pulses and changed the number of π pulses applied in the experiment. For an experiment with a total of N π pulses and one $\pi/2$ pulse and fixed delay time τ, the total evolution time will be $2N\tau$, giving an expected decay in echo size of

$$A = A_0 e^{-2N\tau/T_2}. \tag{4.2}$$

Therefore we measured echo size while varying N in a CPMG experiment and fit the result to a decaying exponential to measure T_2.

Finally, we can also observe Rabi oscillations in our sample using spin-echo

measurements. In section 3.4 we described how we can do this by adding a third pulse before the $\pi/2$ and π pulses, which rotates the spins' states by an angle ϕ_0 away from the z axis of the Bloch sphere. As we increase ϕ_0 gradually the echo will oscillate sinusoidally between its upright and inverted extremes. In section 3.4 we derived the form that we expect these Rabi oscillations to take in the presence of decoherence (equation 3.3). Guided by this result, we measured the echo area for a range of back-pulse durations t and fit the resulting data to the function

$$Y = A_0 e^{-t/K} \cos(\omega_R t + \phi) + c, \tag{4.3}$$

where A_0, K, ω_R, c and ϕ are fit parameters (Figure 4.11). From chapter 2, we expect that ω_R will be related to the amplitude B_1 of the RF oscillating magnetic field by the gyromagnetic ratio:

$$\omega_R = \gamma B_1. \tag{4.4}$$

Thus, using the fit value for ω_R in equation 4.3, we obtained a measurement of the RF magnetic field amplitude in our resonator, finding $B_1 = 5.6$ Oe. This measurement was made using a $10^{-6}\%$ Cr_7Mn sample in deuterated toluene, at a frequency of 4070 MHz.

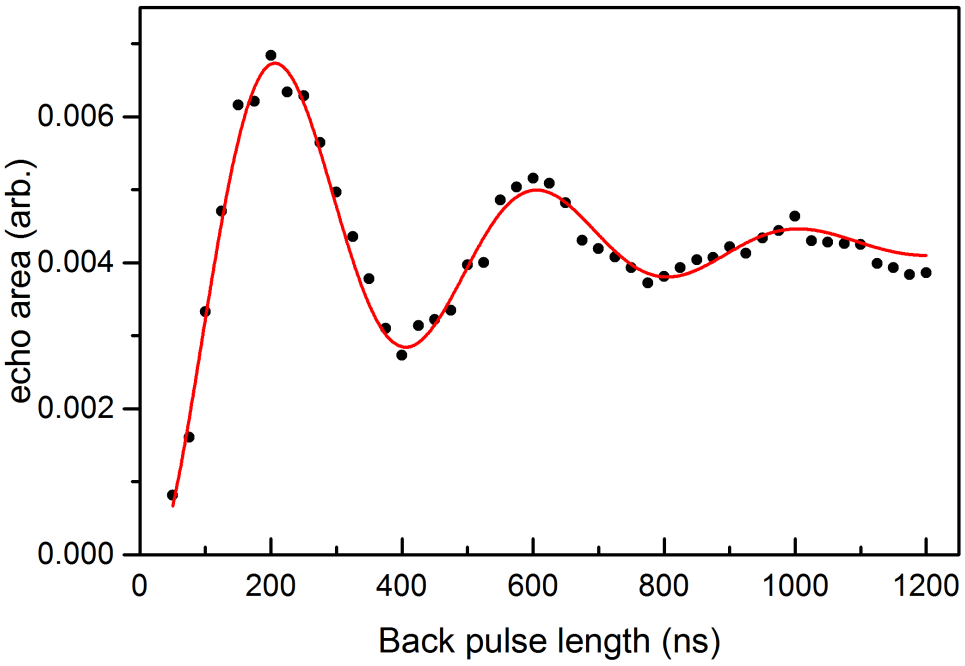

Figure 4.11: Integrated echo signal as a function of pulse duration for a 10^{-6}% Cr_7Mn sample in deuterated toluene. Fitting the resulting Rabi oscillations gives a measurement of the B_1 field in the resonator, which we found to be 5.6 Oe. Measurements taken at 4070 MHz.

Chapter 5

Results and Disucussion

As described in chapter 4, we can measure the coherence time T_2 of our Cr_7Mn samples by conducting spin-echo experiments and varying the delay time between the $\pi/2$ and π pulses. We can then vary parameters of interest such as magnetic field and measure the dependence of T_2 on these parameters. In this chapter we show that we get an enhancement of T_2 near zero external magnetic field, providing strong evidence of an atomic-clock transition, and we show the dependence of T_2 on sample dilution, temperature and properties of the solvent. Finally, we show that we can enhance T_2 by using a Carr-Purcell-Meiboom-Gill pulse sequence instead of the conventional two-pulse Hahn spin-echo sequence.

5.1 Dependence of T_2 on Magnetic Field

We measured the dependence of T_2 on magnetic field and found an enhancement of T_2 when the applied magnetic field is close to zero, as shown in Fig-

ure 5.1 for a 10^{-4}% sample diluted in toluene at 1.9 K. As discussed in section 1.4, this provides strong evidence of an atomic-clock transition at zero field. Enhancement is seen for all sample dilutions and temperatures where we are able to observe a spin echo (see Figures 5.2 and 5.7), and for all solvents we have used (toluene, deuterated toluene, benzene and deuterated benzene, see Figures 5.3 and 5.5).

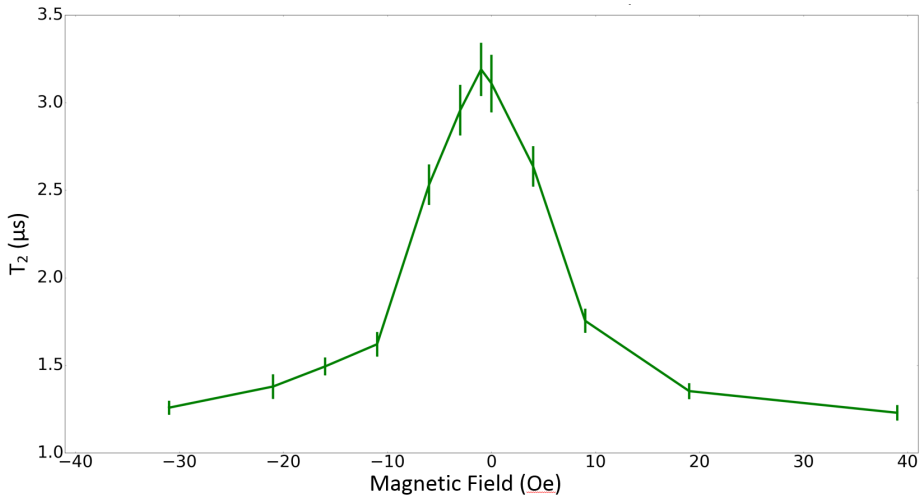

Figure 5.1: The coherence time T_2 of our Cr_7Mn samples increases near zero external magnetic field, as seen in this 0.0001% dilute sample in toluene at 1.9 K, measured with resonator frequency 3975 MHz.

The fact that T_2 is enhanced at a clock transition suggests that dipolar interactions between electron spins and nearby magnetic moments are a limiting factor on coherence time in our samples, since the effect of a clock transition is to reduce sensitivity to these interactions (section 1.4). Shiddiq *et al.* found a similar result in the MNM HoW_{10} [5]. These results show both that dipolar interactions are a limiting factor on coherence times in MNM's (see also [4]) and that the effects of these interactions can be mitigated by working at a

clock transition.

5.2 Dependence of T_2 on Sample Dilution

We measured T_2 as a function of magnetic field for a wide range of sample concentrations, ranging from 1% to 10^{-6}%. As shown in Figure 5.2, T_2 increases at the clock transition between the 1% and 10^{-3}% samples but does not change significantly for more dilute samples. Away from the clock transition dilution seems to have only a small effect on coherence time. Since dilution is also expected to reduce the effects of dipolar interactions, this result suggests that even at the clock transition dipolar interactions limit T_2 for samples more concentrated than 10^{-3}%, but that for more dilute samples they are not a limiting factor. It is therefore somewhat surprising that we see only a small effect of dilution on T_2 away from the clock transition, since the enhancement of T_2 seen at the clock transition suggests that dipolar interactions do limit T_2 away from the transition (section 5.1). If T_2 were limited away from the clock transition by dipolar interactions between neighboring molecules, then more dilute samples should have longer T_2 values. Therefore, the fact that T_2 changes minimally with concentration away from the clock transition suggests that the decoherence away from the clock transition is largely sdue to intramolecular dipolar interactions, that is, interactions with nuclear spins.

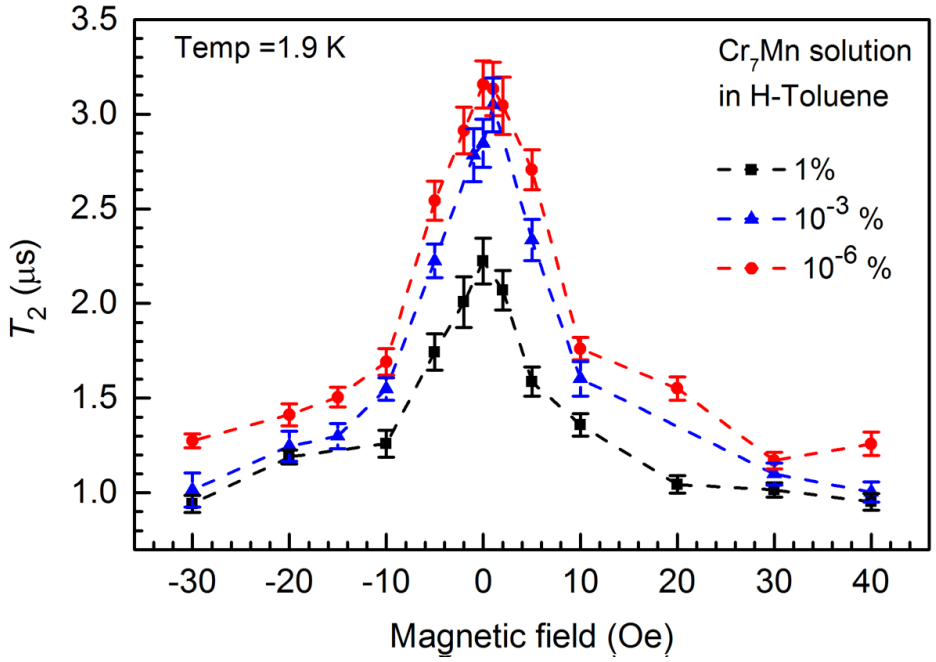

Figure 5.2: Magnetic field dependence of T_2 for Cr_7Mn diluted in toluene at three different concentrations at 1.9 K. Measurements taken at 4076 MHz (1%), 4271 MHz (10^{-3}%) and 3962 MHz (10^{-6}%), respectively.

5.3 Dependence of T_2 on Solvent Properties

We measured T_2 as a function of magnetic field for 10^{-6}% Cr_7Mn samples diluted in regular (hydrogenated) toluene and deuterated toluene and the result is plotted in Figure 5.3. We can see that solvent deuteration has almost no effect on T_2 at the clock transition and although T_2 appears to be slightly higher for the deuterated sample at magnetic fields away from the clock transition, this difference is small enough that it is hard to draw a definitive conclusion. Further, Figure 5.4 shows there is no difference in T_2 between 1% samples in hydrogenated toluene at the clock transition, but seems to show slightly higher T_2 values for the hydrogenated sample away from the transition. Given that

all these differences are small and the apparent differences are not consistent across sample dilutions, it appears that deuteration of toluene has little effect on coherence time in our samples. This result is somewhat surprising given that previous work has shown that using a deuterated toluene solvent can enhance T_2 compared to hydrogenated toluene [10]. However, the result in [10] was measured at a magnetic field of around 0.4 T. and hence far away from any clock transition. The fact that we are working at a clock transition may sufficiently mitigate the effects of dipolar interactions from the solvent that deuteration does not give any significant further improvement. Figure 5.5 shows that we obtained the same result when using benzene as a solvent instead of toluene.

Figure 5.4 also shows a comparison of T_2 between 1% samples diluted in toluene vs. benzene solvent, and we see that the benzene solvent gives a significantly higher T_2 value both at and away from the clock transition. By contrast, Figure 5.6 shows that for much more dilute (10^{-4}%) samples, the choice of benzene or toluene does not appear to change T_2 significantly. This investigation is ongoing and it is not yet clear why benzene solvent should give an improvement T_2 for 1% samples but not for very dilute samples.

5.4 Dependence of T_2 on Temperature

We measured T_2 as a function of the sample temperature for dilute Cr_7Mn samples at a range of different magnetic fields, between temperatures of 1.8 K and 8 K. At temperatures higher than 8 K the signal became too small to

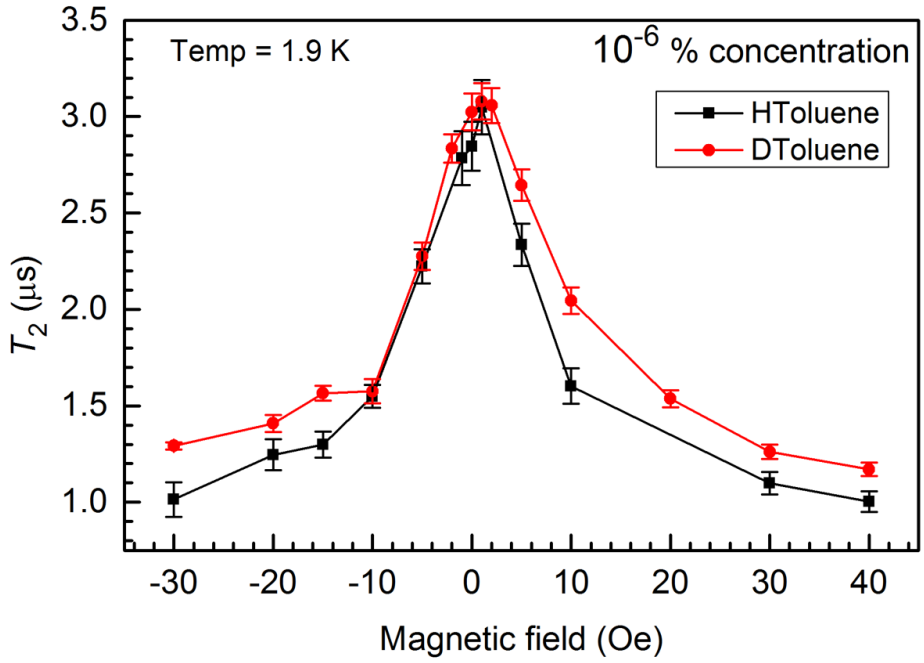

Figure 5.3: Magnetic field dependence of T_2 for 10^{-6}% Cr_7Mn samples diluted in regular (hydrogenated) toluene (black squares) and deuterated toluene (red circles) at 1.9 K. Measurements taken at 3962 MHz and 4102 MHz, respectively.

observe spin echo. Figure 5.7 shows that T_2 decreases with increasing temperature both at the clock transition and 30 Oe away from the transition, where the dependence of T_2 on magnetic field is nearly flat. It also shows that the clock transition still has the effect of increasing T_2, even at the highest temperatures at which we can make measurements.

In Figure 5.8 we show that $1/T_2$ depends linearly on temperature both at and away from the clock transition, and linear fits of these data show that the slope of this linear dependence is similar for the two fields, while the vertical intercepts are different. The fact that $1/T_2$ increases linearly with temperature

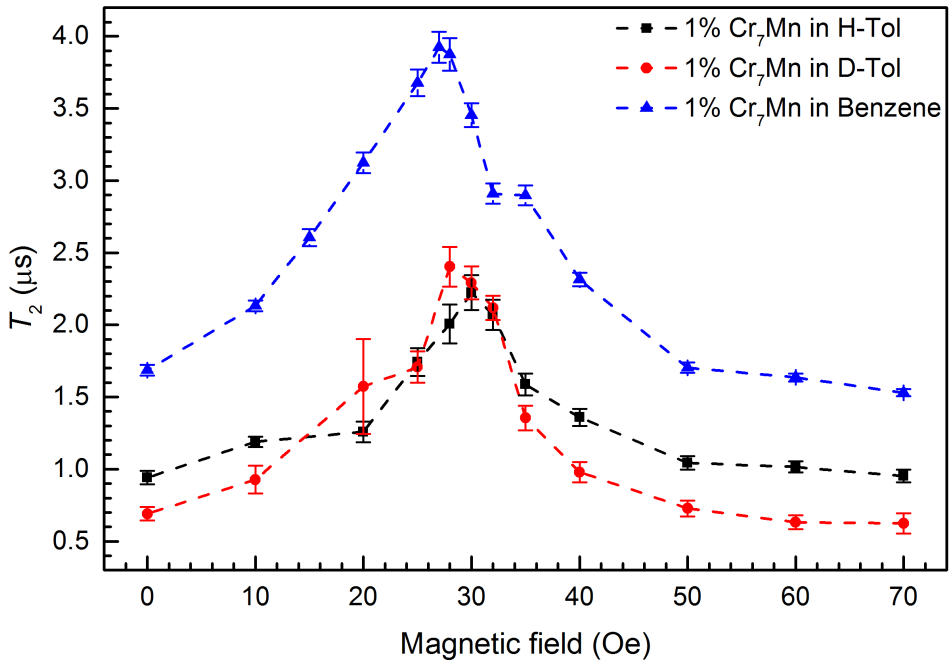

Figure 5.4: Magnetic field dependence of T_2 for 1% Cr_7Mn samples diluted in (hydrogenated) toluene (black squares), deuterated toluene (red circles) and hydrogenated benzene (blue triangles) at 1.9 K. Measurements taken at 4194 MHz, 4076 MHz and 3983 MHz, respectively.

suggests that phonon-mediated decoherence is limiting T_2 in our system.

As given in equation 3.6, we expect the total decoherence rate Γ_{total} due to dipolar interactions and phonon-mediated processes to be the sum of the individual rates from each:

$$\Gamma_{total} = \Gamma_{dipolar} + \Gamma_{phonon}. \tag{5.1}$$

Thus, the difference in vertical intercept at and away from the clock transition in Figure 5.8 is likely due to the fact that the clock transition mitigates the effects of dipolar decoherence, shifting the overall decoherence rate down by a

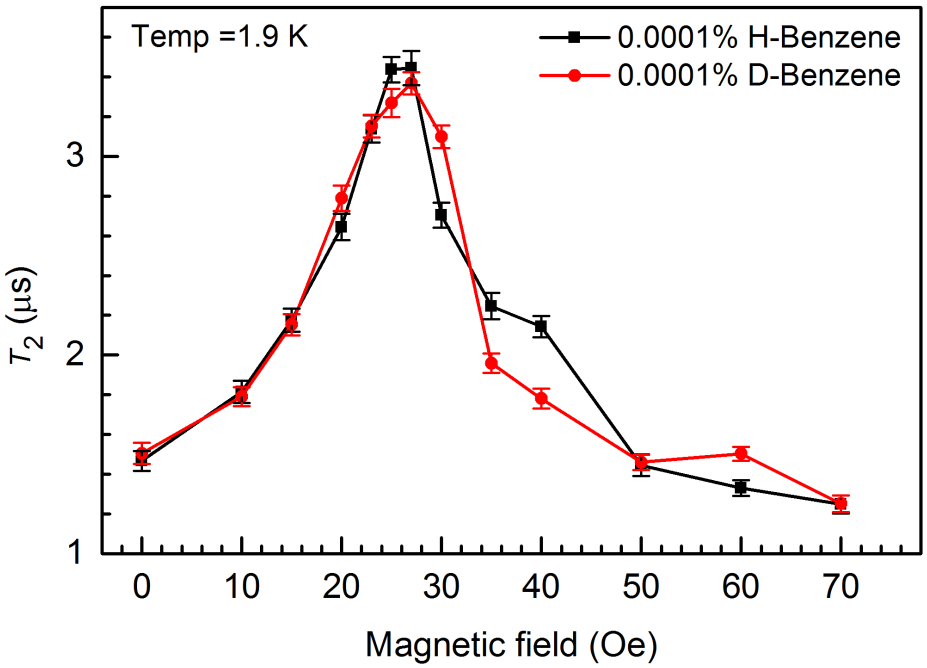

Figure 5.5: Magnetic field dependence of T_2 for 10^{-4}% Cr_7Mn samples diluted in regular (hydrogenated) benzene (black squares) and deuterated benzene (red circles) at 1.9 K. Measurements taken at 4216 MHz and 4242 MHz, respectively.

constant at all temperatures. On the other hand, we do not expect the clock transition to have any effect on decoherence due to phonon-mediated processes, since such processes would be expected to cause decoherence by changing the energy splitting $2E$ of individual molecules rather than by varying the local magnetic field.

Since phonons are bosons, we expect the number, n, of phonons in our system to follow Bose-Einstein statistics. That is, we expect that for a given energy ϵ, we will have

$$n(\epsilon) = \frac{1}{e^{(\epsilon-\mu)/k_BT} - 1}, \tag{5.2}$$

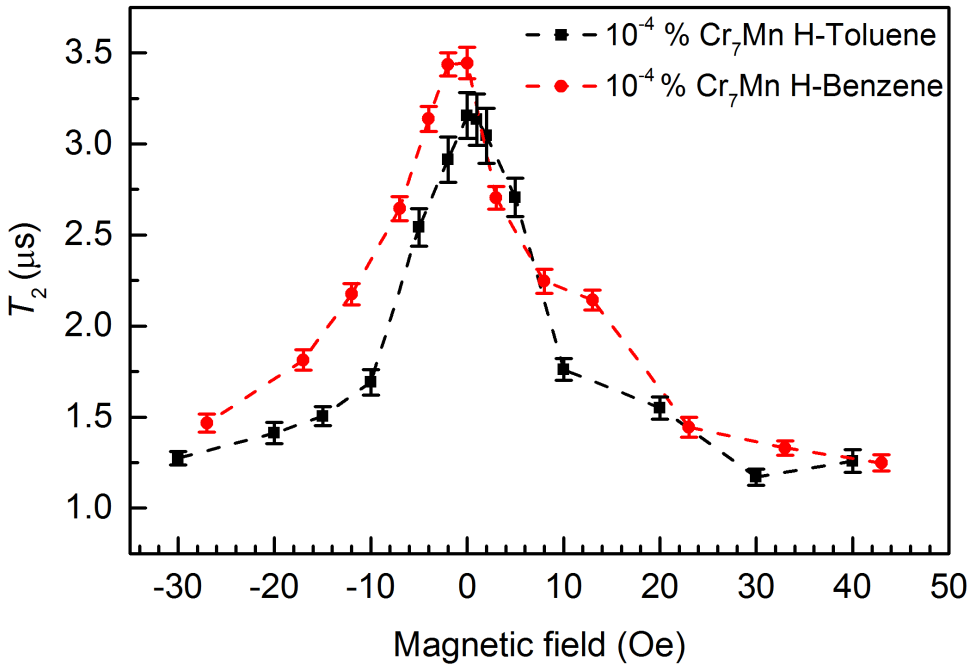

Figure 5.6: Magnetic field dependence of T_2 for 10^{-4}% Cr_7Mn samples diluted in regular toluene (black squares) and regular benzene (red circles) at 1.9 K. Measurements taken at 3975 MHz and 4188 MHz, respectively.

where μ is the chemical potential, k_B is the Boltzmann constant and T is the temperature. For phonons the chemical potential is zero. Let us now examine the high temperature limit of this expression. Note that phonons with very high frequencies will not contribute much to decoherence, since any processes occurring on timescales much faster than the spins' dynamics will have their effects average to zero over the timescales we care about. Therefore, the highest frequencies we care about will be on the order of the transition frequency between the $|+\rangle$ and $|-\rangle$ states. From section 2.2 we know this frequency is $\omega_0 = 2E$, where $E = 1.9$ GHz. Thus we need only consider phonons with energies $\epsilon \lesssim \hbar\omega_0 = 2E\hbar$. Defining $\Delta = \frac{\epsilon}{k_B}$, we see that for the

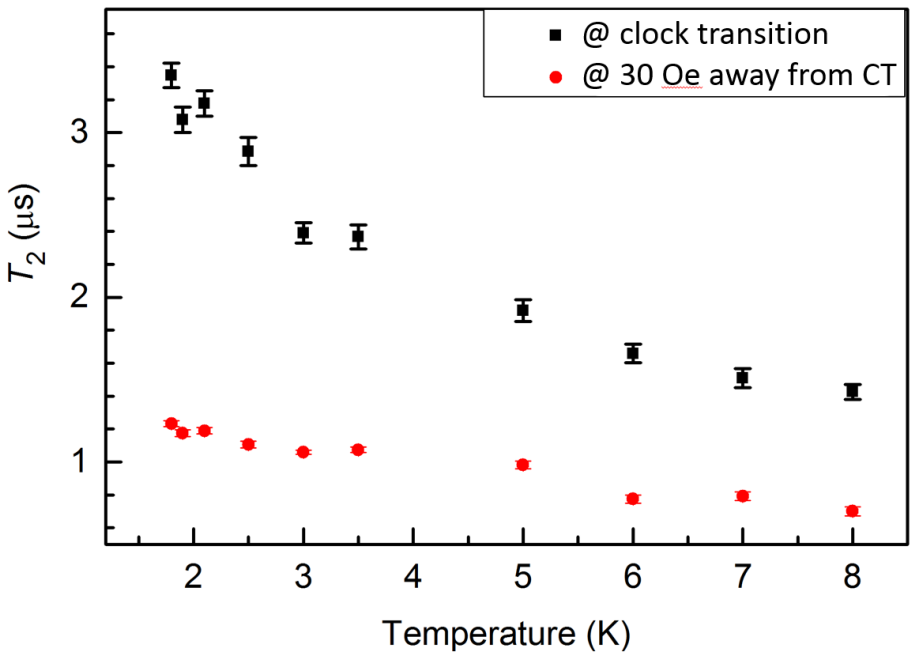

Figure 5.7: T_2 as a function of temperature for 10^{-6}% Cr_7Mn samples diluted in deuterated toluene both at the clock transition (black) and 30 Oe away from the transition (red). Measurements taken at 4070 MHz.

energies we are concerned with, we have $\Delta \lesssim \frac{2E\hbar}{k_B} = 0.029$ K. Since all our experiments are conducted at temperatures of at least 1.8 K, we are clearly working in the high temperature limit of $T >> \Delta$. In this limit, we have

$$e^{\Delta/T} \approx 1 + \Delta/T, \tag{5.3}$$

and hence

$$n(\epsilon) = \frac{1}{e^{\Delta/T} - 1} \approx \frac{1}{\Delta/T} = \frac{T}{\Delta}. \tag{5.4}$$

Equation 5.4 shows that in the high temperature limit we expect the number of phonons at a given energy to scale linearly with temperature. Since the rate

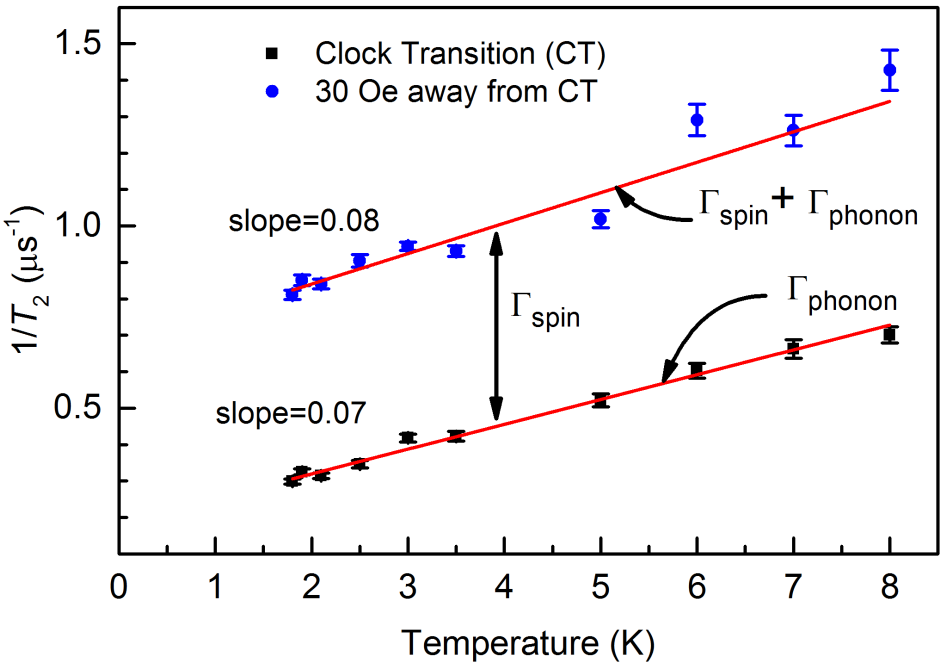

Figure 5.8: Temperature dependence of $1/T_2$ for 10^{-6}% Cr_7Mn samples diluted in deuterated toluene both at the clock transition (black) and 30 Oe away from the transition (blue). Linear fit parameters given for both show similar slopes but different vertical intercepts for the two data sets. Measurements taken at 4070 MHz.

of decoherence due to phonons should also scale linearly with the number of phonons, we expect the decoherence rate to increase linearly with temperature. Thus the linear dependence we found is qualitatively what we expect, although we have not yet done a careful quanitative analysis of this dependence, nor have we yet measured the dependence at lower temperatures. Nonetheless, the fact that the slope of the dependence is similar at and away from the clock transition supports the hypothesis that a phonon-mediated process that acts independently of magnetic field is responsible for decoherence at the clock transition.

5.5 Enhancement of T_2 with CPMG Pulse Sequences

As described in chapters 3 and 4, we used CPMG sequences of up to 50 pulses to refocus spins in our sample, thus correcting for slow decoherence mechanisms. Figure 5.9 shows that use of a CPMG sequence allows us to observe an echo for much longer evolution times than is possible with a standard two-pulse Hahn-echo sequence (see Figure 4.10). Qualitatively, the echo signal disappears well before 10 μs of evolution for standard Hahn spin-echo measurements, while it is still visible at 40 μs for the CPMG experiment. The drop-off in echo signal after 45 μs seen in Figure 5.9 is not present in more recent data taken after cycling the PPMS. We believe this drop-off may have been due to temperature control problems that have now been resolved. More recent data fits better to an exponential decay function but gives very similar results to the T_2 measurements presented here.

Figure 5.10 shows T_2 measured using a CPMG sequence at two magnetic field values (at and away from the clock transition, respectively), as well as the magnetic field dependence of T_2 from a Hahn spin-echo experiment. At both fields, we observe an increase in T_2 by a factor of roughly 2.5. The delay time between consecutive refocusing π pulses in the this experiment was 1100 ns, while the delay time between the $\pi/2$ and π pulses was 550 ns. As discussed in chapter 3, CPMG is expected to mitigate the effects of decoherence mechanisms that occur on a time scale comparable to the delay between pulses, since each successive pulse will refocus the spins on that time

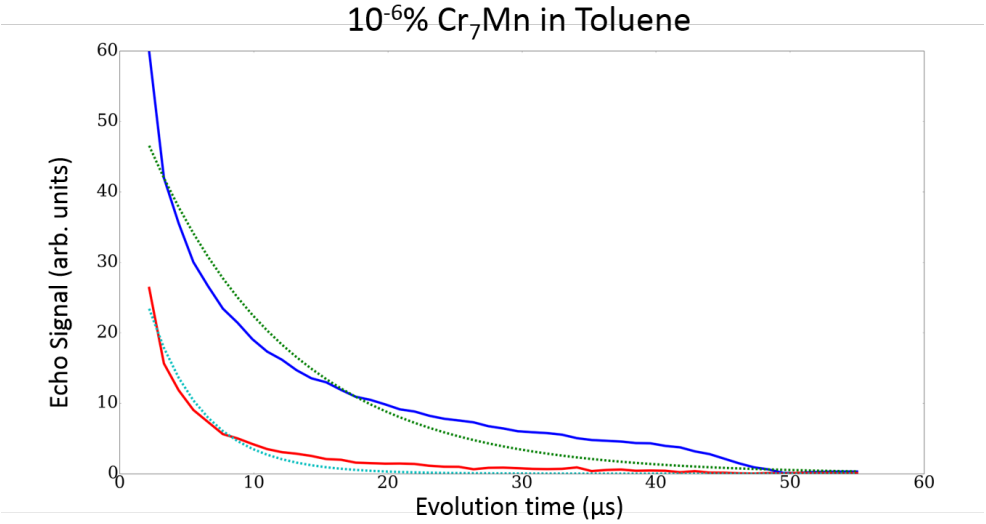

Figure 5.9: Echo decay for CPMG pulse sequences at and away from the clock transition, for a $10^{-6}\%$ sample in deuterated toluene. At the clock transition, an echo can still be seen for evolution times longer than 40 μs. The sharp drop off around 45 μs has been eliminated in more recent experiments.

scale. This suggests that some, but not all, of the decoherence we see is caused by processes that take place on time scales of a few microseconds.

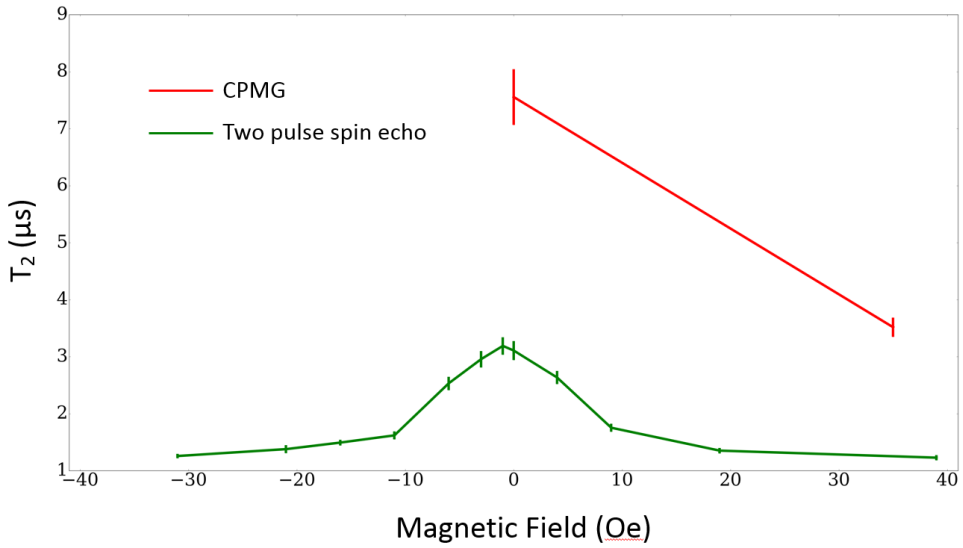

Figure 5.10: Comparison of T_2 vs. magnetic field using CPMG and Hahn echo sequences. The sample concentrations shown here are both below the threshold for T_2 to be independent of dilution (10^{-4}% for the standard spin-echo and 10^{-6}% for the CPMG sequence).

Chapter 6

Conclusion

The goal of this thesis was to characterize the physical processes leading to decoherence in the MNM Cr_7Mn and to identify techniques to mitigate the effects of decoherence. This goal is motivated both by an inherent interest in studying decoherence mechanisms in quantum systems and by the potential applications for MNM's in quantum computing applications, which would require long enough coherence times to permit high-fidelity gate operations.

We first demonstrated the ability to measure T_2 in our Cr_7Mn molecules by conducting spin-echo experiments and observing the decay in echo size with evolution time. This allowed us to measure T_2 while varying parameters such as magnetic field, temperature, sample dilution and solvent properties. We found that T_2 was enhanced at zero magnetic field, providing strong evidence for an atomic-clock transition, where the spins' states are immune to first order from fluctuations in local magnetic field. The result that T_2 is enhanced at a clock transition suggests that dipolar interactions with neighboring spins

are a limiting factor on coherence times in our system. Further supporting this conclusion is the fact that reducing our sample concentration from 1% to 10^{-3}% increased T_2 values at the clock transition. At lower concentrations we saw only small changes from the 10^{-3}% samples, suggesting that we have reached the dilute limit in which dipolar interactions between molecules are not a major limiting factor on T_2.

We also attempted to test whether dipolar interactions with spins in the solvent (toluene or benzene) were limiting T_2. We found no perceptible effect of solvent deuteration at the clock transition, although there appeared to be a small effect away from the transition. We also got very similar results between toluene and benzene, with the one important difference being that in benzene T_2 did not appear to change significantly with concentration for concentrations up to 1%, in contrast the results in toluene. Hence we can conclude that dipolar interactions with spins in the solvent are not a major limiting factor on T_2, although further investigation is required.

Finally, we found that T_2 increases at low temperatures, with $1/T_2$ scaling linearly with temperature with roughly the same slope at and away from the clock transition. This suggests that the temperature dependence of T_2 is not due to dipolar interactions, but rather to phonon-mediated interactions that will not be affected by the clock transition. Moreover, the vertical intercept of the dependence was higher away from the transition, consistent with our expectation that dipolar interactions will contribute more to decoherence away from the transition, thus shifting the decoherence rate up by a constant at all temperatures.

Thus, we have succeeded in isolating the effects of two different decoherence mechanisms and identified the factors that affect each mechanism, allowing us to reduce decoherence from each mechanism independently. We were also able to learn something about the rate of some sources of decoherence by conducting CPMG experiments. Specifically, we found an increase in T_2 by about a factor of three relative to the result from the standard Hahn spin-echo procedure, both at and away from the clock transition when using CPMG pulse sequences with pulse spacing on the order of 1 μs. This suggests that a significant portion of decoherence processes in our system occur on timescales of microseconds to tens of microseconds.

The results of this work suggest many possible directions for future experiments, several of which could be conducted fairly easily with the techniques and apparatus developed for this project. Firstly, we would like to extend our study of temperature dependence to include temperatures at least an order of magnitude lower than 1.8 K, the lowest achievable temperature with the PPMS. Since our samples and resonators are easily transportable, this could be done using a dilution fridge in another lab. As described in section 5.4, the decoherence rate $1/T_2$ should scale linearly with the number of phonons in our system, which we expect to follow a Bose-Einstein distribution. Therefore, it would be informative to see whether the linear dependence observed thus far is indeed the high temperature limit of such a distribution or whether other decoherence mechanisms come into play at low temperatures.

We would also like to further explore CPMG and other dynamical decoupling procedures such as concatenated dynamical decoupling [31] [32] to char-

acterize the noise spectrum in our experiments. Our most recent data does not show the sudden drop-off in echo signal signal seen in Figure 5.9, and we therefore plan to next fully characterize the dependence of T_2 on temperature and other parameters of interest using CPMG sequences.

In addition, there are many experiments that could easily be conducted using slight variations on our Cr_7Mn molecules or solvents that would further probe the decoherence mechanisms in our experiments. For instance, Ardavan *et al.* [10] observed an increase in T_2 when using deuterated Cr_7Ni samples and it would be interesting to see whether a similar effect is observed in Cr_7Mn and especially at the clock transition. Another interesting experiment would be to use a variant of Cr_7Mn with a more rigid bond structure, which may reduce the effects of phonon-mediated processes since individual molecules would be less susceptible to vibrations, leading to less variation in the energy splitting $2E$ over time. We have already contacted Richard Winpenny's group about the possibility of preparing such samples in the near future.

With only slight modifications to our existing apparatus, we should be able to observe two-photon transitions between the $|+\rangle$ and $|-\rangle$ states, provided we can get a strong enough RF magnetic field at the sample location during the pulses. The results of our Rabi experiments (section 5.6) suggest an RF field amplitude of 5.6 Oe in the loop when using our thickest resonator. We could likely get even larger amplitudes by acquiring an additional amplifier or carefully designing a new resonator.

One final exciting direction for this project would be to use dimers of Cr_7Mn to construct a two-qubit quantum logic gate, as described briefly in chapter 1.

This has already been investigated by another thesis student, Michael Cha, this year, with some promising results, and in this thesis we have shown that we can achieve long enough coherence times to make basic gate operations feasible. Nonetheless, there are many obstacles remaining, including the questions of whether dimer samples will maintain their coupling when dissolved in toluene or benzene and how we can design a resonator and pulse sequences to interact with both molecules in a dimer in the same experiment.

Thus our study of decoherence mechanisms in Cr_7Mn has proved to be a fruitful endeavor and suggests other possible experiments, many of which are quite feasible with slight modifications to our current techniques. We have already achieved coherence times that could make Cr_7Mn an attractive candidate for applications in quantum computing and paved the way for further investigations of decoherence mechanisms in MNM's. It is my hope that this work will lead to more research into decoherence mechanisms and quantum computing applications in MNM's.

Chapter 7

Appendix A

Here I give an example calculation showing how to prepare dilute samples of Cr_7Mn. Suppose we want to prepare a sample using m grams of Cr_7Mn crystal. The density of Cr_7Mn is $\rho = 0.582\ g/cc$, so the volume of this crytal sample will be

$$V_c = \frac{m}{\rho} \tag{7.1}$$

Then to prepare a 1% solution (by volume), for example, we want to use a volume V_s of solvent such that

$$\frac{1}{100} = \frac{V_c}{V_s + V_c} \approx \frac{V_c}{V_s} = \frac{m}{\rho V_s}, \tag{7.2}$$

where the approximation in the second equality is good for very dilute samples, since then $V_s >> V_c$. Solving for V_s then gives

$$V_s = \frac{100m}{\rho} \tag{7.3}$$

Now suppose we later want to make a more dilute sample. Since it is difficult to measure out very small amounts of Cr_7Mn powder, we do this by further diluting a portion of our existing 1% sample. For two samples with the same quantity of Cr_7Mn powder and different volumes of solvent, V_1 and V_2, the concentrations C_1 and C_2 of the two samples respectively will be related by

$$\frac{C_1}{C_2} = \frac{V_2}{V_1}. \tag{7.4}$$

Thus, given a desired sample concentration and an existing sample with known concentration and volume, we can use equation 7.4 to find the volume of solvent we should add to make the new sample.

Bibliography

[1] C. A. Collett, K.-I. Ellers, N. Russo, K. R. Kittilstved, G. A. Timco, R. E. Winpenny, and J. R. Friedman, "A clock transition in the cr7mn molecular nanomagnet," *Magnetochemistry*, vol. 5, no. 1, p. 4, 2019.

[2] G. Timco, S. Marocchi, E. Garlatti, C. Barker, M. Albring, V. Bellini, F. Manghi, E. J. McInnes, R. G. Pritchard, F. Tuna, W. Wernsdorfer, G. Lorusso, G. Amoretti, S. Carretta, M. Affronte, and R. E. P. Winpenny, "Heterodimers of heterometallic rings," *Dalton Transactions*, vol. 45, no. 42, pp. 16610–16615, 2016.

[3] QuantumDesign, "Physical property measurement system: Hardware manual," 2000.

[4] T. D. Ladd, F. Jelezko, R. Laflamme, Y. Nakamura, C. Monroe, and J. L. O′Brien, "Quantum computers," *Nature*, vol. 464, no. 7285, p. 45, 2010.

[5] E. Knill and R. Laflamme, "Theory of quantum error-correcting codes," *Physical Review A*, vol. 55, no. 2, p. 900, 1997.

[6] C. Neill, P. Roushan, K. Kechedzhi, S. Boixo, S. V. Isakov, V. Smelyanskiy, A. Megrant, B. Chiaro, A. Dunsworth, K. Arya, R. Barends, B. Bur-

kett, Y. Chen, Z. Chen, A. Fowler, B. Foxen, M. Giustina, R. Graff, E. Jeffrey, T. Huang, J. Kelly, P. Klimov, E. Lucero, J. Mutus, M. Neeley, C. Quintana, D. Sank, A. Vainsencher, J. Wenner, T. C. White, H. Neven, and J. M. Martinis, "A blueprint for demonstrating quantum supremacy with superconducting qubits," *Science*, vol. 360, no. 6385, pp. 195–199, 2018.

[7] C. Negrevergne, T. S. Mahesh, C. A. Ryan, M. Ditty, F. Cyr-Racine, W. Power, N. Boulant, T. Havel, D. G. Cory, and R. Laflamme, "Benchmarking quantum control methods on a 12-qubit system," *Physical Review Letters*, vol. 96, p. 170501, May 2006.

[8] K. A. Landsman, T. S. C. Figgatt, N. M. Linke, B. Yoshida, N. Y. Yao, and C. Monroe, "Verified quantum information scrambling," *Physical Review B*, vol. 597, pp. 61–65, 2019.

[9] J. I. Colless, V. V. Ramasesh, D. Dahlen, M. S. Blok, M. Kimchi-Schwartz, J. McClean, J. Carter, W. De Jong, and I. Siddiqi, "Computation of molecular spectra on a quantum processor with an error-resilient algorithm," *Physical Review X*, vol. 8, no. 1, p. 011021, 2018.

[10] A. Ardavan, O. Rival, J. J. L. Morton, S. J. Blundell, A. M. Tyryshkin, G. A. Timco, and R. E. P. Winpenny, "Will Spin-Relaxation Times in Molecular Magnets Permit Quantum Information Processing?," *Physical Review Letters*, vol. 98, p. 057201, Jan. 2007.

[11] M. Shiddiq, D. Komijani, Y. Duan, A. Gaita-Arino, E. Coronado, and

S. Hill, "Enhancing coherence in molecular spin qubits via atomic clock transitions," *Nature*, vol. 531, no. 7594, p. 348, 2016.

[12] J. Medford, C. Barthel, C. Marcus, M. Hanson, A. Gossard, *et al.*, "Scaling of dynamical decoupling for spin qubits," *Physical Review Letters*, vol. 108, no. 8, p. 086802, 2012.

[13] C. J. Wedge, G. Timco, E. Spielberg, R. George, F. Tuna, S. Rigby, E. McInnes, R. Winpenny, S. Blundell, and A. Ardavan, "Chemical engineering of molecular qubits," *Physical Review Letters*, vol. 108, no. 10, p. 107204, 2012.

[14] L. M. Vandersypen and I. L. Chuang, "Nmr techniques for quantum control and computation," *Reviews of modern physics*, vol. 76, no. 4, p. 1037, 2005.

[15] J. R. Friedman and M. P. Sarachik, "Single-molecule nanomagnets," *Annu. Rev. Condens. Matter Phys.*, vol. 1, no. 1, pp. 109–128, 2010.

[16] P. Santini, S. Carretta, F. Troiani, and G. Amoretti, "Molecular nanomagnets as quantum simulators," *Physical Review Letters*, vol. 107, p. 230502, Nov 2011.

[17] M. Leuenberger and D. Loss, "Quantum computing in molecular magnets," *Nature*, vol. 410, pp. 789–93, 05 2001.

[18] A. Gaita-Arino, F. Luis, S. Hill, and E. Coronado, "Molecular spins for quantum computation," *Nature chemistry*, vol. 11, pp. 301–309, 2019.

[19] A. L. Barra, D. Gatteschi, and R. Sessoli, "High-frequency epr spectra of a molecular nanomagnet: Understanding quantum tunneling of the magnetization," *Physical Review B*, vol. 56, no. 13, p. 8192, 1997.

[20] M. L. Baker, S. J. Blundell, N. Domingo, and S. Hill, "Spectroscopy methods for molecular nanomagnets," in *Molecular nanomagnets and related phenomena*, pp. 231–291, Springer, 2014.

[21] D. N. Woodruff, R. E. Winpenny, and R. A. Layfield, "Lanthanide single-molecule magnets," *Chemical reviews*, vol. 113, no. 7, pp. 5110–5148, 2013.

[22] E. Garlatti, T. Guidi, S. Ansbro, P. Santini, G. Amoretti, J. Ollivier, H. Mutka, G. Timco, I. Vitorica-Yrezabal, G. Whitehead, R. E. P. Winpenny, and S. Carretta, "Portraying entanglement between molecular qubits with four-dimensional inelastic neutron scattering," *Nature communications*, vol. 8, p. 14543, 2017.

[23] J. H. Atkinson, A. D. Fournet, L. Bhaskaran, Y. Myasoedov, E. Zeldov, E. del Barco, S. Hill, G. Christou, and J. R. Friedman, "Effects of uniaxial pressure on the quantum tunneling of magnetization in a high-symmetry mn_{12} single-molecule magnet," *Physical Review B*, vol. 95, p. 184403, May 2017.

[24] W. Wernsdorfer and R. Sessoli, "Quantum phase interference and parity effects in magnetic molecular clusters," *Science*, vol. 284, no. 5411, pp. 133–135, 1999.

[25] W. Wernsdorfer, N. Aliaga-Alcalde, D. N. Hendrickson, and G. Christou, "Exchange-biased quantum tunnelling in a supramolecular dimer of single-molecule magnets," *Nature*, vol. 416, no. 6879, p. 406, 2002.

[26] A. Ardavan, A. M. Bowen, A. Fernandez, A. J. Fielding, D. Kaminski, F. Moro, C. A. Muryn, M. D. Wise, A. Ruggi, E. J. McInnes, K. Severin, G. A. Timco, C. R. Timmel, F. Tuna, G. F. Whitehead, and R. E. Winpenny, "Engineering coherent interactions in molecular nanomagnet dimers," *npj Quantum Information*, vol. 1, p. 15012, 2015.

[27] J. S. Townsend, *A modern approach to quantum mechanics*. 2 ed.

[28] C. E. Shannon, "Communication in the presence of noise," *Proceedings of the IEEE*, vol. 72, no. 9, pp. 1192–1201, 1984.

[29] E. L. Hahn, "Spin echoes," *Physical review*, vol. 80, no. 4, p. 580, 1950.

[30] G. A. Rinard and G. R. Eaton, "Loop-gap resonators," in *Biomedical EPR, Part B: Methodology, Instrumentation, and Dynamics*, pp. 19–52, Springer, 2005.

[31] K. Khodjasteh and D. Lidar, "Fault-tolerant quantum dynamical decoupling," *Physical Review Letters*, vol. 95, no. 18, p. 180501, 2005.

[32] W. Witzel and S. D. Sarma, "Concatenated dynamical decoupling in a solid-state spin bath," *Physical Review B*, vol. 76, no. 24, p. 241303, 2007.